

Kelvin-Helmholtz versus Tearing Instability: What Drives Turbulence in Stochastic Reconnection?

GRZEGORZ KOWAL,¹ DIEGO A. FALCETA-GONÇALVES,¹ ALEX LAZARIAN,² AND ETHAN T. VISHNIAC³

¹*Escola de Artes, Ciências e Humanidades
Universidade de São Paulo
Av. Arlindo Béttio, 1000 – Vila Guaraciaba
CEP: 03828-000, São Paulo - SP, Brazil*

²*Department of Astronomy
University of Wisconsin,
475 North Charter Street,
Madison, WI 53706, USA*

³*Department of Physics & Astronomy
Johns Hopkins University
3400 N. Charles Street
Baltimore, MD 21218, USA*

Submitted to ApJ

Abstract

Over the last few years it became clear that turbulent magnetic reconnection and magnetized turbulence are inseparable. It was not only shown that reconnection is responsible for violating the frozen-in condition in turbulence, but also that stochastic reconnection in 3D generates turbulence by itself. The actual mechanism responsible for this driving is still unknown. Processes such as tearing mode or Kelvin–Helmholtz, among other plasma instabilities, could generate turbulence from irregular current sheets. We address the nature of the driving mechanism for this process and consider a relative role of tearing and Kelvin–Helmholtz instabilities for the process of turbulence generation. In particular, we analyze the conditions for development of these two instabilities within three-dimensional reconnection regions. We show that both instabilities can excite turbulence fluctuations in reconnection regions. However, tearing mode has a relatively slow growth rate, and at later times it becomes partially suppressed by the transverse component of the magnetic field, generated during the growth of turbulent fluctuations. On the contrary, the Kelvin–Helmholtz instability establishes quickly in the outflow region, and at later times it dominates the turbulence generation compared to the contribution from tearing mode. Our results demonstrate that the tearing instability is subdominant compared to the Kelvin–Helmholtz instability in terms of generation of turbulence in the 3D reconnection layers and therefore the self-driven reconnection is turbulent reconnection with tearing instability being important only at the initial stage of the reconnection.

Keywords: magnetic reconnection — turbulence — magnetohydrodynamics (MHD) — methods: numerical

1. INTRODUCTION

Magnetic reconnection is a fundamental problem essential for understanding the magnetohydrodynamic (MHD) flows, especially turbulent ones. Within such

flows magnetic flux tubes cross each other and therefore the properties of the flow depend on whether the tubes can or cannot cross each other.

The answer that follows from the Sweet–Parker theory of magnetic reconnection (Parker 1957; Sweet 1958) is that in typical astrophysical situations the magnetic flux tubes cannot reconnect and change the magnetic field topology. Indeed, the Sweet–Parker reconnection

rate is $V_{\text{rec,SP}} \approx V_A S_L^{-1/2} \ll V_A$ with $S_L = LV_A/\eta$ being the Lundquist number, L - a longitudinal scale of the reconnecting flux tube, V_A - the Alfvén speed, and η - the magnetic resistivity. Given the large scales of magnetic fields involved in astrophysical flows and the highly conductive nature of astrophysical plasmas, it is obvious that S_L is so large that the rates predicted by the Sweet–Parker mechanism are absolutely negligible. This, however, is in gross contradiction with observational data, e.g., the data on Solar flares. The Sweet–Parker reconnection is an example of a slow laminar reconnection, while one requires much faster reconnection to explain observations. Formally, the fast reconnection is one that does not depend on S_L or, if depends, depends on it logarithmically.

For years the fast reconnection research was focused on the X-point reconnection, i.e. the reconnection at which magnetic field is brought at a sharp angle in the reconnection zone. This is opposed to the Sweet-Parker reconnection which is an example of the Y-point reconnection. The X-point reconnection was proposed by Petschek (1964) and required that the inflow and outflow of the matter into reconnection zone are comparable. Indeed, the slow rate of reconnection with Y-point can be viewed as a direct consequence of the disparity of the scale of astrophysical inflow of the fluid and the scale of outflow determined by microphysics, i.e., the resistivity or plasma effects, the latter, however, challenged by Lazarian & Vishniac (1999, henceforth LV99).

The most significant point of the LV99 theory was that in the presence of the three-dimensional (3D) turbulence, the reconnection outflow is determined by the magnetic field wandering and the width of the outflow is the function of turbulence intensity rather than the resistivity of plasma effects¹. The predicted by the LV99 theory dependence of the reconnection rate on the level of turbulence was successfully tested in the numerical studies of Kowal et al. (2009, 2012). More recently, these predictions received an additional support from relativistic MHD simulations by Takamoto et al. (2015). The most important consequence of the LV99 theory,

¹ The LV99 proposal was radically different from earlier suggestions of enhancing the reconnection rate by turbulence. For instance, Jacobson & Moses (1984) considered effect of turbulence on micro-scales by increasing Ohmic resistivity. Obviously, this could provide the change of the Sweet-Parker rate only by an insignificant factor. Similarly, 2D simulations of turbulence in Matthaeus & Lamkin (1985, 1986) could not shed light on the actual 3D physics of magnetic reconnection. Indeed, the component of magnetic field responsible for the wandering in LV99 model is the Alfvénic mode. This mode is absent in 2D simulations. Thus these works were appealing to the X-points that are produced by turbulence.

contrary to all the previous theories of fast reconnection, was the prediction that the reconnection does not require special settings, but happens everywhere in turbulent media. As a result, this violates flux freezing in astrophysical fluids, which are generically turbulent (see Eyink 2011; Eyink et al. 2011). This remarkable break down of the classical magnetic flux freezing theorem (Alfvén 1942) was numerically demonstrated in Eyink et al. (2013)².

Turbulence can be both, externally driven, as it is testified from the observations of the ISM and molecular clouds (see Armstrong et al. 1995; Padoan et al. 2009; Chepurnov & Lazarian 2010; Chepurnov et al. 2015), but it can also be driven by the reconnection process as first discussed in LV99 and further elaborated in Lazarian & Vishniac (2009). The first numerical study of magnetic reconnection induced by turbulence that is generated by reconnection were performed in Beresnyak (2013) with an incompressible code, and later in Oishi et al. (2015) and Huang & Bhattacharjee (2016) taking into account compressibility. A detailed numerical study of reconnection with self-generated turbulence was performed in Kowal et al. (2017).

One of the most important questions of the current research on 3D reconnection faces the nature of turbulence in the reconnection events. Our earlier study in Kowal et al. (2017) demonstrated that the turbulence generated in the reconnection events follows the Goldreich–Sridhar statistics (Goldreich & Sridhar 1995). However, an open issue is related to the driving mechanism of the observed turbulent motions. The literature has suggested that tearing modes, plasmoid instabilities, and shear-induced instabilities could mediate the energy transfer from coherent to turbulent flows. The issue of the relative importance of different driving processes has not been explored quantitatively.

In our numerical experiments we do not identify tearing modes, although filamentary plasmoid-like structures are present. Visual inspection shows, however, that their filling factor is small. Sheared flows, on the other hand, are present around and within the whole current sheet. As the field lines reconnect, the Lorentz force increases, accelerating plasma and creating the current sheet. This process is patchy and bursty in 3D. Therefore, the accelerated flows are strongly sheared. The statistical importance of these burst flows is large, as already shown in our previous work (Kowal et al.

² The violation of flux freezing in turbulent fluids entails an important effect of reconnection diffusion that has big consequences, changing the paradigm of magnetically controlled star formation (see Lazarian 2005; Santos-Lima et al. 2010; Lazarian et al. 2012).

2017), as we compared the velocity anisotropy of reconnecting events to that of decaying turbulence without the reversed field. The Kelvin–Helmholtz instability due to the sheared velocities in reconnecting layers has already been conjectured as possible origin of turbulence by Beresnyak (2013). In Kowal et al. (2017), we provided the solid evidence for the self-generated turbulence driven by the velocity shear. Here we perform a proper analysis of the growth-rates of such instabilities.

Velocity shear is a global process that occurs in regular magnetized and unmagnetized fluids. The nonlinear evolution of the related instabilities, such as Kelvin–Helmholtz instability, is known to be one of the main contributors to the energy transfer between wave modes, i.e., the energy cascade. If the energy cascade in reconnection layers is led by similar mechanisms, it is straightforward to understand why the statistics observed resemble those of Kolmogorov-like turbulence, and Goldreich–Sridhar anisotropy scaling. In other words, our claim is that the turbulent onset and cascade in reconnection is not different to those found in regular MHD and hydrodynamic systems.

In this work we consider two possible instabilities both extensively studied analytically and numerically since 1960s, namely tearing mode instability in a slab geometry (see Furth et al. 1963; Somov & Verneta 1989), which naturally develops in a thin elongated current sheets, and Kelvin–Helmholtz instability (see, e.g. Chandrasekhar 1961; Michalke 1964; Fejer 1964; Sen 1964; Gerwin 1968; Ong & Roderick 1972; Miura & Pritchett 1982; Frank et al. 1996; Faganello & Califano 2017; Berlok & Pfrommer 2019), which could result from the local velocity shear produced by the outflows from reconnection sites. Both instabilities are able to generate turbulence near current sheets. In this work we investigate which one is responsible for or dominates the generation of turbulence in stochastic reconnection, i.e. the reconnection without an externally imposed turbulence resulting from a weak initial plasma irregularities.

In what follows we provide a brief review of theoretical analysis of Kelvin–Helmholtz and tearing instabilities in §2, together with dispersion relations derived for different magnetic field and velocity profiles and conditions for their suppression. In §3, we describe numerical simulation and our approach in analyzing both instabilities. In §4 we present the results of our analyses and compare the maximum growth rates of the two instabilities at different times, which we discuss in §5. Finally, in §6 we state our conclusions.

2. ANALYZED INSTABILITIES

2.1. Tearing Mode Instability

With tokamaks in mind, many works on tearing mode instability considered a cylindrical plasma column in so called “pinch configuration” or simply toroidal geometry. In such a configuration, the current density pinch, due to the change of the azimuthal component of magnetic field, is located at some distance from the column center and the axial component is usually stronger than the azimuthal one (see, e.g. Coppi et al. 1976; Ara et al. 1978). In this subsection we briefly review the dispersion relations for tearing mode derived in a slab geometry, where one component of magnetic field changes the sign over a short distance 2δ along its perpendicular direction. It is known that independently of the configuration, the plasma is stable in the ideal MHD framework. The stability occurs once a finite resistivity is taken into account.

Furth et al. (1963) developed a theory of resistive MHD instabilities for the case of the neutral current layer with an arbitrary magnetic field profile. However, in derivation of the dispersion relations they considered a piecewise linear or hyperbolic tangent profiles. From their theory, we know that the tearing mode develops under condition $\alpha = k\delta < 1$, where k is the perturbation wavenumber (along the sheet plane) and δ is the current sheet half-width (see Table 1 in Furth et al. 1963). Under the assumption of the so called “constant Ψ ” in the region of discontinuity (see §5 in Furth et al. 1963), where Ψ is the flux function of the in-plane magnetic field, $\vec{B} = (-\partial_y \Psi, \partial_x \Psi)$, the growth rate γ , expressed by the renormalized growth rate $p = \gamma\tau_R$, of the instability for the piecewise linear profile is given by

$$p \approx \alpha^{-2/5} S^{2/5} \quad (1)$$

with $S = \tau_R/\tau_A$, where $\tau_R = 4\pi\delta^2/\eta$ is the resistive diffusion time, $\tau_A = \delta/v_A$ is the Alfvén time, and $v_A = B_0/\sqrt{4\pi\rho_0}$ is the upstream Alfvén speed. This growth rate corresponds to short-wavelength modes, $\alpha S^{1/4} \ll 1$. For the long-wavelength modes, $\alpha S^{1/4} \gg 1$, the function Ψ is no longer constant in the region of discontinuity and the dispersion relation takes form

$$p \approx \alpha^{2/3} S^{2/3}. \quad (2)$$

The existence of these two regimes with different scalings indicates that the growth rate of tearing mode has its maximum p_{max} with respect to α , which according to Furth et al. (1963) scales as $p_{max} \sim S^{1/2}$. Coppi et al. (1976), analyzing the internal kink instability of a plasma column, and Loureiro et al. (2007), considering a finite length current sheet, derived complete dispersion relations covering both regimes.

The tearing mode usually is studied in the two-dimensional (2D) incompressible MHD framework, and

since the theory by [Furth et al. \(1963\)](#) there was search for additional mechanism which could stabilize or destabilize ever more the instability. [Furth et al. \(1963\)](#) already considered effects of fluid compressibility, thermal conductivity or finite viscosity concluding that they do not affect the instability. Nevertheless, the tearing instability is a subject to suppression under some circumstances. For instance, the presence of traverse, i.e. normal to the current sheet plane, magnetic field component stabilizes tearing mode. The stabilization effect of this component was demonstrated by [Schindler \(1974\)](#) and [Galeev & Zeleniy \(1975, 1976\)](#).

[Somov & Verneta \(1989\)](#) have shown that the stabilization effect of the transverse field B_n becomes to be essential when $\xi \equiv B_n/B_0 \geq S^{-3/4}$, decreasing the growth rate p with increasing the value of ξ . Once $\xi \gg S^{-3/4}$, the instability is completely stabilized. They derived the dispersion relation for the tearing instability in the presence of B_n , which is given by

$$\Delta^{1/4} \left(\frac{\alpha^2 S^2}{p} \right)^{1/4} \left(1 - \frac{p^{3/2}}{\alpha S} \Delta^{-1/2} \right) - p\alpha \sqrt{\frac{\pi}{2}} = 0, \quad (3)$$

where $\Delta = (1 + \xi^2 S^2/p)^{-1}$. The above dispersion relation is valid for $\xi < \alpha$. Once $\xi \rightarrow 0$ ($\Delta \rightarrow 1$), Eq. (3) reduces to

$$\left(\frac{\alpha^2 S^2}{p} \right)^{1/4} \left(1 - \frac{p^{3/2}}{\alpha S} \right) - p\alpha \sqrt{\frac{\pi}{2}} = 0, \quad (4)$$

properly recovering the scalings in the short- and long-wavelength regimes discussed before. Applying an implicit derivative to Eq. (3) with respect to α and setting $dp/d\alpha = 0$ provides the following relationships between the maximum growth rate p_{max} and the corresponding α_{max}

$$\alpha_{max} = \frac{2}{\sqrt[3]{\pi}} \left(\frac{p_{max}}{S^2} + \xi^2 \right)^{1/6} \quad \text{and} \quad p_{max} = \left(\frac{\pi^2}{64} \alpha_{max}^6 - \xi^2 \right) S^2. \quad (5)$$

Inserting the equation for α_{max} into the dispersion relation Eq. (3) gives us an expression for the maximum growth rate p_{max} , which depends only on ξ and S ,

$$p_{max}^4 + \xi^2 S^2 p_{max}^3 - \frac{1}{\pi} \left(\frac{2}{3} \right)^3 S^2 = 0. \quad (6)$$

The resulting expression is a quartic function which has negative determinant for any possible value of ξ , thus it has two real roots, one negative and one positive, with the positive one being the physical maximum growth rate. Provided the estimates of ξ and S from the simulations, we can therefore determine the maximum growth

rate p_{max} . For $\xi = 0$ this equation gives directly the maximum growth rate $p_{max} = (2/3)^{3/4} \pi^{-1/4} S^{1/2}$ compatible with the estimate given by [Furth et al. \(1963\)](#). Once p_{max} is determined, we can also retrieve the corresponding parameter α_{max} from the left expression in Eq. (5), from which we can calculate the wavenumber $k_{max} = \alpha_{max}/\delta$ at which the maximum growth rate p_{max} takes place.

2.2. Kelvin–Helmholtz Instability

The Kelvin–Helmholtz instability can develop in a region of velocity shear. Following [Chandrasekhar \(1961, §XI, Eq. 204\)](#), we can write its growth rate γ for an incompressible flow, assuming equal density on both sides and perturbation parallel to the shear direction, as

$$\gamma = k \sqrt{U^2 - v_A^2}, \quad U > v_A \quad (7)$$

where U is the velocity shear amplitude, assuming it changes from $-U$ to U between two layers, v_A is the local Alfvén speed and k is the wavenumber of perturbation. This expression, however, is valid only for a simplified case of a “vortex sheet”, where the velocity has a discontinuity in the sheet location, and gives unrealistic growth rate, increasing with k to arbitrarily large values. A more realistic continuous shear layer was already considered long time before. In the hydrodynamic framework, [Rayleigh \(1879\)](#) derived a dispersion relation for a linear piecewise profile of velocity. Also [Chandrasekhar \(1961\)](#) considered continuous variations of density and velocity profiles (see §102–104 and Fig. 120 there), while [Michalke \(1964\)](#) analyzed numerically an hyperbolic tangent profile. All these works concluded that the growth rate reaches its maximum value γ_{max} for $k_{max}\delta < 1$, where δ is the half-width of the shear region. Following [Rayleigh \(1879\)](#) derivation, [Drazin & Reid \(1981, see §23\)](#) provided the growth rate for the Kelvin–Helmholtz instability with a piecewise linear velocity profile in the hydrodynamic framework,

$$\gamma^2 = \frac{U^2}{4\delta^2} \left[e^{-4\alpha} - (1 - 2\alpha)^2 \right], \quad (8)$$

where $\alpha \equiv k\delta$. The expression indicates that the instability is completely stabilized for $\alpha \gtrsim 0.639$, and the maximum growth rate occurs at $\alpha \approx 0.398$. In the incompressible MHD framework, [Ong & Roderick \(1972\)](#), considering also a piecewise linear profile, derived the following dispersion relation

$$\Omega^4 + \Omega^2 \left[\alpha - 2\alpha^2 (1 + 1/\mathcal{M}_A^2) - \frac{1}{4} (1 - e^{-4\alpha}) \right] + \alpha^4 (1 - 1/\mathcal{M}_A^2)^2 - \alpha^3 (1 - 1/\mathcal{M}_A^2) + \frac{1}{4} \alpha^2 (1 - e^{-4\alpha}) = 0, \quad (9)$$

where $\Omega = \omega\delta/U$, $\mathcal{M}_A^2 = U^2/v_A^2$ is the Alfvénic Mach number related to the shear amplitude U , and $\omega = \phi + i\gamma$, with ϕ and γ being the phase change and growth rate, respectively. The dispersion relation expressed by Eq. (9) is valid, however, in the limit $\mathcal{M}_A^2 \gg 1$ for $\alpha \leq 1.0$. In the hydrodynamic limit, i.e., once \mathcal{M}_A tends to infinity, the dispersion relation becomes compatible with the relation provided by [Drazin & Reid \(1981\)](#). Similar analytical studies of magnetized Kelvin-Helmholtz instability with a linear velocity profile were done by [Gudkov & Troshichev \(1996\)](#) resulting in compatible conclusions.

[Ong & Roderick \(1972\)](#) also studied the Kelvin-Helmholtz instability in the compressible MHD framework. In this regime, they derived the following dispersion relation

$$\begin{aligned} 8\alpha\mu^2\Omega^4 + \Omega^2 \left[-4 + \mu^2 \left(-1 - 4\alpha + 8\alpha^2 - \frac{10}{8}\alpha^3 \right) \right] \\ + (1 - 2\alpha)^2 - e^{-4\alpha} \\ - \mu^2 \left(\alpha^2 - \frac{4}{3}\alpha^3 - \frac{8}{3}\alpha^4 + \frac{8}{5}\alpha^5 \right) = 0, \quad (10) \end{aligned}$$

valid when $\mu^2 \equiv \mathcal{M}^2/\alpha^2 \ll 1$ with $\mathcal{M} = U/c_M$, $c_M = \sqrt{a^2 + v_A^2}$, and a being the magnetosonic Mach number, the magnetosonic speed, and the sound speed, respectively. Once $\mu^2 \rightarrow 0$, Eq. (10) reduces to the relation compatible with Eq. (8). Both above dispersion relations (Eqs. 9 and 10) indicate the existence of the maximum growth rate γ_{max} at corresponding wavenumber k_{max} also in the magnetized version of the Kelvin-Helmholtz instability, with $k_{max}\delta \lesssim 1$. In order to find γ_{max} and k_{max} , one has to solve these relations numerically for a given δ , U , v_A , and a , which is somewhat simplified since both equations are biquartic functions.

[Miura & Pritchett \(1982\)](#) studied the Kelvin-Helmholtz instability numerically in a general configuration, i.e., taking into account the compressibility and arbitrary angles between the shear direction, magnetic field and perturbation propagation. They derived a sufficient condition for stability, $U \leq v_A \left(\vec{k} \cdot \hat{B}_0 \right) / \left(\vec{k} \cdot \hat{U} \right)$ which, assuming that the perturbation wavevector \vec{k} and magnetic field \vec{B}_0 both lay in the plane of the maximum shear and form angles ϕ and θ with the shear direction, respectively, can be written as

$$U \leq v_A (\cos \theta + \sin \theta \tan \phi). \quad (11)$$

The condition states that if the magnetic field is aligned with the shear ($\vec{B}_0 \parallel \vec{U}$, i.e. $\theta = 0$), the angle of the perturbation propagation ϕ does not matter and the mode is stable if $U \leq v_A$. Once the magnetic field is perpendic-

ular to the shear ($\vec{B}_0 \perp \vec{U}$, i.e. $\theta = 90^\circ$), the perturbations are stabilized only for modes nearly perpendicular to the shear ($\phi \approx 90^\circ$). Moreover, considering the perturbation propagating strictly along the shear ($\vec{k} \parallel \vec{U}$), for the perpendicular field ($\vec{B}_0 \perp \vec{U}$), the instability develops only if $\mathcal{M} < 1$, which is equivalent to $U < c_M$. For the parallel magnetic field ($\vec{B}_0 \parallel \vec{U}$), the instability is completely suppressed for $\mathcal{M}_s = U/a > 1$, once $\mathcal{M}_A > 1$ has to be fulfilled for instability.³ However, the restrictions for \mathcal{M} and \mathcal{M}_s are relaxed for perturbations propagating obliquely with respect to the sheared velocity component and magnetic field (see Eq. 37 in [Miura & Pritchett 1982](#)). Moreover, it is important to notice that even though the system may be strongly magnetized overall, in the regions where reconnection occurs the local degree of magnetization decreases considerably, allowing the growth of KH-unstable modes (see, e.g., [Loureiro et al. 2013](#)).

3. METHODOLOGY AND MODELING

3.1. Numerical Simulations

In this work we analyze a numerical simulation of the reconnection-driven turbulence in a 3D rectangular domain with physical dimensions $L \times 4L \times L$ (with assumed $L = 1$) by solving non-ideal isothermal compressible magnetohydrodynamic equations using a high-order shock-capturing adaptive refinement Godunov-type code AMUN⁴. The exact numerical setup of the model analyzed here is the same as of the models presented in [Kowal et al. \(2017\)](#), with the sound speed $a = 1.0$ ($\beta = 2.0$), and explicit viscosity ν and resistivity η , both equal to 10^{-5} , in order to control the effects of numerical diffusion. The model was ran with the base resolution of $32 \times 128 \times 32$, and the local mesh refinement up to 7 levels, with the refinement criterion based on the normalized value of vorticity and current density, resulting in the effective resolution $2048 \times 8192 \times 2048$ or the effective grid size $h = 1/2048$ (the same for all directions). The initial density ρ_0 and the strength of reconnecting component of magnetic field B_0 were set to unity, resulting in the velocity and the simulation time units being $[v] = V_A = 1$ and $[t] = t_A = L/V_A = 1$, respectively. It is important to note, that the code works with the normalized magnetic field multiplied by a factor of $\sqrt{4\pi}$. Therefore, the Alfvén speed using the code units is given by $V_A = B_0/\sqrt{\rho_0}$. In addition to the reconnecting magnetic field component along the X-direction, we

³ [Miura & Pritchett \(1982\)](#) considered the velocity change from $-V_0/2$ to $V_0/2$ and calculated Mach numbers using V_0 resulting in respective conditions for Mach numbers $\mathcal{M}_s < 2$ and $\mathcal{M}_A > 2$.

⁴ The code is freely available from <http://amuncode.org>

also set the uniform guide field along the Z-direction of the strength of 0.1. The velocity field was initiated with fluctuations represented by 100 Fourier modes of random phases and directions, the amplitude equal to 10^{-2} and the fixed wavenumber of $k = 64\pi$. The simulation was terminated after $t = 7.0$. For a complete description of the numerical setup of the model, the boundary conditions and numerical methods used please refer to Kowal et al. (2017).

3.2. Shear Detection in Vector Fields

In order to detect locations of the current sheet we analyze a quantity which is correlated with the local change of the polarization of magnetic field, or simply the magnetic shear. There are several techniques proposed in the literature to determine locations where the reconnection takes place. The most straightforward is the amplitude of current density $|\vec{J}|$. We can also use the magnetic shear angle, i.e. the change of the magnetic field direction along a line, or the Partial Variance of Increments method (PVI) which measures the variation of the magnetic field across the current sheet (see Greco et al. 2008; Servidio et al. 2011). Similarly, for the velocity shear, we can consider, for example, the vorticity $\vec{\omega} = \nabla \times \vec{v}$ as the shear detector. In this work we analyze the local maximums of the euclidean norm of the shear rate tensor $S_{ij} = \partial u_i / \partial x_j + \partial u_j / \partial x_i$ for $i \neq j$ and $S_{ij} = 0$ for $i = j$, $S = \|S_{ij}\| \equiv \sqrt{\sum_{ij} S_{ij}^2}$, where $x_i, x_j \in \{x, y, z\}$ and \vec{u} means either \vec{B} or \vec{v} , depending on the analyzed instability. Therefore, $S = S(x, y, z)$ is a function of position.

Our algorithm to determine the local geometry of the shear consists of the following steps:

1. At each domain cell $\vec{p} = (x, y, z)$ we calculate the 2^{nd} order partial derivatives of $S(x, y, z)$ along each direction, $\partial_x^2 S$, $\partial_y^2 S$, and $\partial_z^2 S$ in order to verify if the position is a local maximum. The type of maximum is determined by the number of negative 2^{nd} order derivatives. In a given point of the 3D domain, one, two or three negative 2^{nd} order derivatives identify a sheet-like, ridge-like, or peak-like local maximums, respectively. In our analysis, we consider all types of the local maximums, requiring that at least one derivative is negative. If all derivatives are non-negative, the remaining steps of analysis are skipped and the next cell is considered. This guarantees that the next computationally expensive steps are avoided for cells which do not lay in the regions of shear maximums.
2. For each cell of the local shear maximum, i.e., the cell which has at least one negative 2^{nd} order derivative determined in the previous step, we calculate the complete Hessian of the analyzed shear detector S

$$H_{ij}^J = \frac{\partial^2 S}{\partial x_i \partial x_j}, \quad (12)$$

where again $x_i, x_j \in \{x, y, z\}$. By solving the eigenproblem for the Hessian, we can get the direction of the steepest decay of S at the given location, which is determined by the eigenvector $\hat{e}_n = \hat{e}(\lambda_{\min})$ corresponding to the minimum eigenvalue $\lambda_{\min} = \min\{\lambda_i\}$. The previous step guarantees the existence of at least one negative eigenvalue.
3. The eigenvector \hat{e}_n is perpendicular to the component which suffers the strongest shear. However, we would like to determine a complete vector base corresponding to the directions along the strongest shear, \hat{e}_s , across that shear, \hat{e}_n , and perpendicular to both, $\hat{e}_g = \hat{e}_n \times \hat{e}_s$ (see the left panel of Fig. 1). Since a pure shear is a combination of the normal stress and rotation, is it not trivial to determine its precise direction. Moreover, in a generic case, the stress may not be planar, acting along all three principal axes. In order to deal with such a situation, we can assume that we are only interested in a plane defined by two principal axes, corresponding to the strongest positive and strongest negative normal stresses. In order to determine them, we need to solve the eigenproblem for the shear rate tensor S_{ij} . The eigenvector, \hat{e}_g , corresponding to the middle eigenvalue determines the plane of the maximum shear. Therefore, the direction of the sheared component \hat{e}_s is
$$\hat{e}_s = \hat{e}_n \times \hat{e}_g. \quad (13)$$

There is no reason for \hat{e}_n and \hat{e}_g to be perfectly orthogonal. Therefore, after normalizing \hat{e}_s , \hat{e}_n is corrected by setting it to $\hat{e}_s \times \hat{e}_g$. This completes the determination of the orthonormal base of the shear.
4. After determining our orthonormal base in the local shear maximum, we perform the interpolation of all three components of the analyzed vector field, u_x , u_y , and u_z along the normal direction determined by vector \hat{e}_n within a distance of several cell sizes (e.g., $s = -20h, \dots, 20h$, where s is the distance in the units of cell size h). Projecting the resulting vectors on \hat{e}_s we obtain the sheared

component of the analyzed vector field,

$$u_s(s) = \hat{e}_s \cdot \vec{u}(\vec{p} + s\hat{e}_n). \quad (14)$$

For the interpolation, we use a piecewise quintic Hermite interpolation which preserves the continuity of the first and second derivatives (see, e.g., Dougherty et al. 1989).

5. At this point we perform fitting of the sheared component $u_s(s)$ to the hyperbolic tangent function $f(s) = \delta u \tanh[(s - s_0)/\delta] + u_0$ (or a piecewise linear function) to the obtained profile $u_s(s)$. The fitting is done within the region $s_l \leq s \leq s_u$, where $s_l < 0$ and $s_u > 0$, and s_l and s_u indicate distances along \hat{e}_s at which the derivative du_s/ds changes sign. The estimated values δu , u_0 correspond to the amplitudes of the sheared and uniform components, respectively, s_0 is the shift with respect to the current position, and δ is the half-width of the profile. The right panel in Figure 1 shows an example of the determined sheared component of magnetic field $B_s(s)$ together with its fitting (blue and dashed red lines, respectively). The fitting parameters are shown in the title of the plot.
6. Along the normal direction, \hat{e}_n , we can also project other quantities. For example, in the case of the tearing mode we estimate the transverse component of magnetic field $B_n(s) = \hat{e}_n \cdot \vec{B}(\vec{p} + s\hat{e}_n)$. By averaging $B_n(s)$ within the local current sheet, i.e. within the interval $s_l \leq s \leq s_u$ of the fitted function, we can get the mean value of the transverse component of magnetic field $\langle B_n \rangle$. Similarly, the upstream Alfvén speed can be determined from, e.g., $v_A = \hat{e}_n \cdot [\vec{v}_A(\vec{p} - \delta\hat{e}_n) + \vec{v}_A(\vec{p} + \delta\hat{e}_n)]/2$, which is necessary to estimate the Lundquist number S .
7. Finally, in order to estimate the length of the shear region, i.e. the longitudinal dimension of the shear, we project the detector S along the vector parallel to the sheared component of the field, $S(s) = S(\vec{p} + s\hat{e}_s)$, and analyze the decay of S along s . We measure the distance l between points where S drops to a half of its maximum value in position \vec{p} , treating l as the longitudinal length of shear region.

The procedure described above allows us to estimate the thickness δ and the longitudinal dimension l of all shear regions found in the domain. For each region we can determine the local direction of the shear \hat{e}_s and estimate other parameters required for determination of

the local growth rate γ , which are described more in the next subsection.

For illustration, in the left panel of Figure 1 we show a sketch of a shear region (with arbitrary orientation) with vector field lines of the opposite polarization (red and blue) with the local reference frame used to project the field components on three axes \hat{e}_s , \hat{e}_n , and \hat{e}_g , corresponding to the shear, transverse and guide components. For the case of magnetic shear, an extracted profiles of sheared (reconnecting) $B_s(s)$, transverse $B_n(s)$, and guide $B_g(s)$ components (blue, orange, and green respectively) along the direction normal to the current sheet are shown in the right panel of Figure 1. The plot also shows the fitted parameters δB , B_0 and δ of the sheared component (red dashed line) together with the estimated stabilizing parameter ξ .

3.3. Estimation of Conditions and Growth Rates for Tearing Instability

The estimation of the growth rate of tearing mode in fluid simulations is not trivial. First of all, it is necessary to detect the locations of current sheets, and once it is done, to estimate the local Lundquist number S from the upstream Alfvén speed v_A and the thickness δ of each sheet region. In order to take into account the effect of transverse field, we need to estimate ξ from the transverse and total magnetic fields, B_n and B , respectively. Nevertheless, all these parameters are not sufficient enough since we still need information about the local perturbations, which might be especially difficult to characterize. In the turbulent case, considered here, we usually have a packet of waves of different amplitudes, wavenumbers and directions traveling through the considered region. First of all, we can estimate the bounds for the perturbation wavenumber k from the current sheet region geometry. Estimating the longitudinal length of the sheet, l , (see step 7 in the previous section), we can determine the lower limit for the wavenumber $k_l \approx 2\pi/l$. The upper wavenumber limit is determined by the resolution of the simulation, i.e., $k_h \approx 2\pi/h$. Therefore, the permitted range of wavenumbers for local perturbations is $k_l \lesssim k \lesssim k_h$. For our analysis, it is enough, however, to consider k_{max} corresponding to the maximum growth rate γ_{max} assuming, that since we have a turbulent region, there is a high probability finding fluctuations with wavenumber equal to k_{max} present in the region. Obviously, if k_{max} lays out of the permitted range, the limited value of $k_{max} = \min(\max(k_{max}, k_l), k_h)$ should be considered in the estimation of the tearing growth rate γ_{max} . Also, we take into account that $k_{max}\delta$ should be smaller than unity.

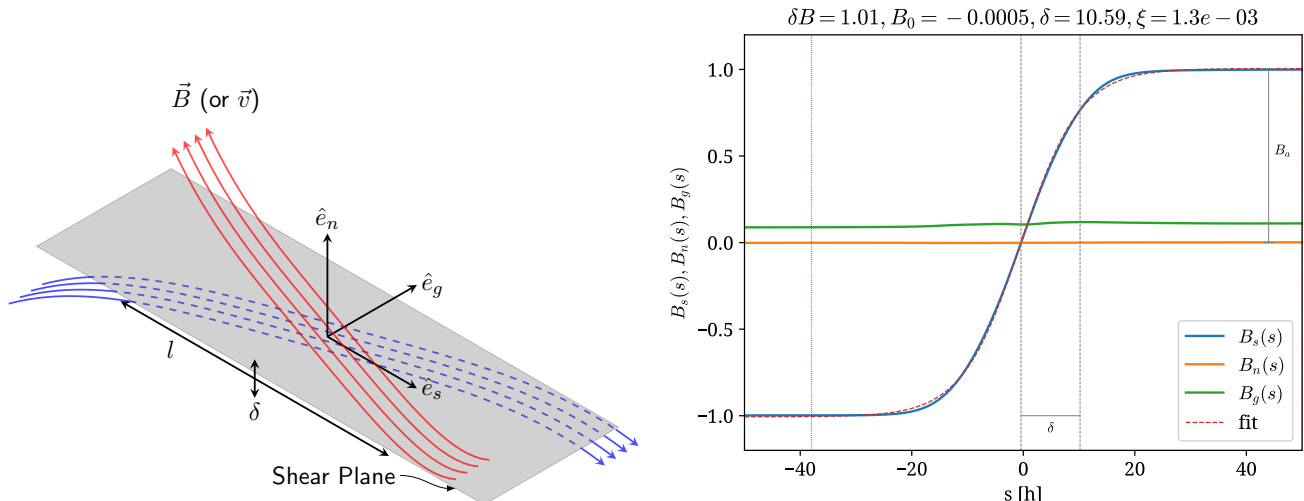


Figure 1. *Left:* Sketch of a shear region with the local reference frame indicating directions of the shear \hat{e}_s , transverse (normal) \hat{e}_n , and guide components \hat{e}_g of the analyzed vector field (\vec{B} or \vec{v} field). The length l of the shear region and its thickness δ are determined along \hat{e}_s and \hat{e}_n axes, respectively. *Right:* Example profiles of the shear (reconnecting), transverse and guide components of magnetic field (B_s , B_n , and B_g , respectively) projected on the direction normal to current sheet in one of the selected points of the detected current sheet. The estimated parameters of the fitting of the reconnecting component $B_s(s)$ are shown in the title. The horizontal scale is in the units of the effective cell size h .

For the case of tearing instability, the algorithm described in §3.2 allows us to determine the thickness of local current sheet δ , the local upstream Alfvén speed v_A , the transverse and total components of magnetic field, B_n and B , respectively, and the longitudinal scale of sheet region l . From δ and v_A we calculate S (using the explicit value of resistivity η for which the simulation was done), and from B_n and B we calculate ξ . The estimated values of S and ξ are inserted into Eq. (6), which is solved numerically in order to get p_{max} . Then, using the left expression in Eq. (5) we estimate α_{max} from p_{max} . If $\alpha_{max} = k_{max}\delta < k_l\delta$, however, its value is limited by setting $\alpha_{max} = k_l\delta$ and estimating p numerically directly from Eq. (3) for a given $\alpha = \alpha_{max}$, using, e.g., the Newton iterative root finder with the initial guess set p_{max} obtained from Eq. (6). In this way we estimate the local growth rate of tearing instability, $\gamma_{max} = p_{max}/\tau_R$, and the corresponding wavenumber k_{max} . The results of this analysis are presented in §4.1 and §4.3.

3.4. Estimation of Conditions and Growth Rates for Kelvin–Helmholtz Instability

The Kelvin–Helmholtz instability is analyzed in a similar manner as the tearing mode. Here, we determine the positions of the velocity shear using the algorithm described in §3.2. Once a shear region is detected, its thickness δ and longitudinal dimension l are estimated. These two parameters allow us to estimate the permitted range of the wavenumbers of perturbation, $k_l \lesssim k \lesssim k_h$, where k_l and k_h are calculate in the same way as in the tear-

ing instability, i.e., $k_l = 2\pi/l$, and $k_h = 2\pi/h$, however, l refers here to the longitudinal dimension of the velocity shear region. From 11 we see that the stability condition depends on the relative angle between the direction of perturbation propagation $\hat{k} = \vec{k}/k$, the direction of local magnetic field $\hat{B}_0 = \vec{B}_0/B_0$, both with respect to the direction of shear $\hat{U} = \vec{U}/U$. Discussing the distribution of U in §4.2 we consider two cases, $\vec{k} \parallel \vec{B} \parallel \vec{U}$ and $\vec{k} \parallel \vec{B} \perp \vec{U}$. However, in the derivation of maximum growth rates described below we always assume the case of three vectors parallel to each other.

In order to determine the growth rate of the Kelvin–Helmholtz instability in each detected region, we estimate the shear velocity $U = \delta v_s$ from the interpolated transverse component of velocity (see step 5 in §3.2). We also estimate the upstream Alfvén speed v_A in a similar way as in the tearing mode. In this way we build a vector of samples for the shear width δ , the velocity shear amplitude U , and the Alfvén speed v_A , necessary to verify the stability conditions and estimate the growth rate from Eqs. (7), (9), and (10). In estimating the maximum growth rate γ_{max} in the case of discontinuous shear and incompressible MHD (Eq. 7) we estimate the wavenumber k_{max} from the condition $k_{max} = \max(0.4/\delta, k_l)$. The value 0.4 has been chosen based on the $k_{max}\delta$ for the piecewise linear profile for the hydrodynamic case (see Eq. 8 and the description below). In the case of MHD Kelvin–Helmholtz instability dispersion relations with the piecewise linear profile (Eqs. 9 and 10), both α_{max} and Ω_{max} have to be found numerically using, for exam-

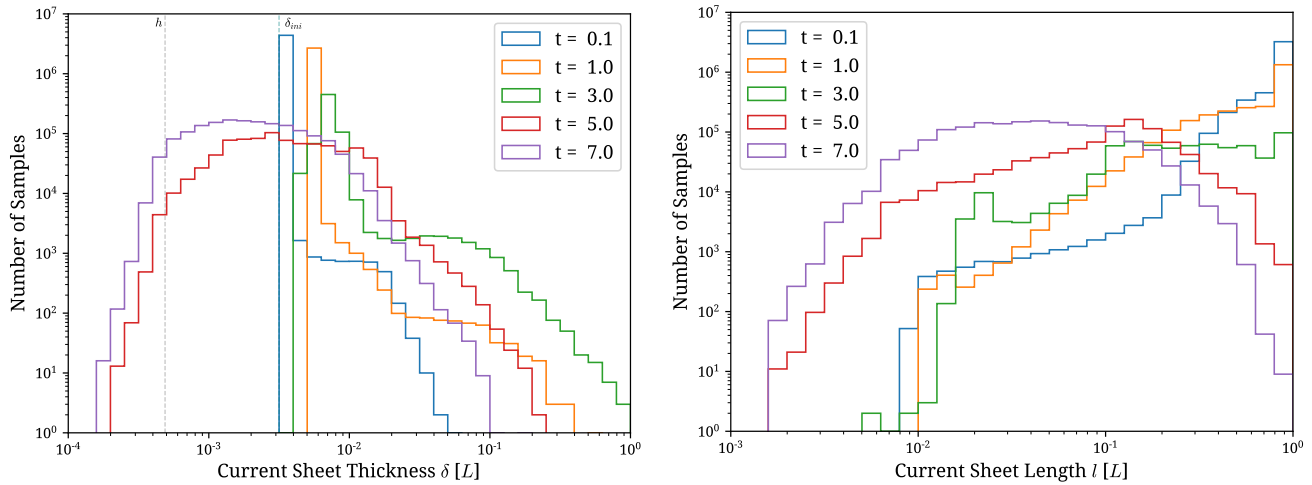


Figure 2. Statistics of the current sheet thickness δ (left) and length l (right) for different evolution moments, $t = 0.1, 1.0, 3.0, 5.0, 7.0$ (blue, orange, green, red, and purple, respectively). The right vertical dashed line (teal) shows the initial thickness of current sheet $\delta_{ini} = 3.16 \times 10^{-3}$, and the left line (grey) shows the effective grid size h .

ple, the golden section method (Kiefer 1953). Once they are estimated, we calculate the maximum growth rate from $\gamma_{max} = \text{Im}(\Omega_{max})U/\delta$ and $k_{max} = \alpha_{max}/\delta$. The results of the above described analysis of the Kelvin–Helmholtz instability are presented in §4.2 and §4.3.

4. ANALYSIS AND RESULTS

Before we describe our results, we should stress, that we present the statistical results corresponding to the populations of cells which belong to magnetic (current sheet) or velocity shear maximums and not individual shear regions. It means that we do not group cells as belonging to the same shear region or not, or analyze any connectivity between these cells. It also does not mean, that we demonstrate the statistics of individual shear regions. The number of samples shown in, e.g., histograms, has only comparative, and not absolute meaning, and since we analyze cells at shear maximums, it should not be interpreted as a filling factor, once divided by the total effective number of cells in the system. The main objective of this work is to verify what conditions are provided for the development of analyzed instabilities in the reconnection-driven turbulence, and if they can be responsible for energy input driving local turbulence.

4.1. Tearing instability analysis

Before we estimate the growth rate of tearing instability, we shall analyze the properties of current sheets in the system. From Eqs. (1) and (2) we see, that the growth rate γ increases with the decrease of the current sheet thickness δ . It also increases with the perturbation wavenumber k for $k < k_{max}$ (i.e., for long-wavelength modes), and decreases with k for $k > k_{max}$

(i.e., for short-wavelength modes). These two quantities, δ and k , also determine the instability condition $k\delta < 1$. Therefore, we will analyze them first.

In the left plot of Figure 2 we show the distribution of current sheet thicknesses δ for all detected current sheet cells at times $t = 0.1, 1.0, 3.0, 5.0$, and 7.0 . Two vertical lines correspond to the effective cell size $h = 1/2048$ (left) and the initial current sheet thickness $\delta_{ini} = 3.16 \times 10^{-3}$. We see that at initial times two populations of samples corresponding to current sheet regions form. The first dominating one is characterized by thickness which broadens to values several times larger than the initial thickness δ_{ini} , and the second one characterized by very broad current sheets with δ comparable to a fraction of the unit length L (see, e.g., green line in Fig. 2 corresponding to $t = 3.0$). The population of broad current sheets seems to be transient, since at $t = 5.0$ (red line in Fig. 2) it is significantly suppressed. For $t \geq 5.0$, the distribution is not characterized by two populations anymore, and it shifts to smaller values of δ with a significant fraction of the detected current sheet samples comparable or below the effective cell size h , indicating a sharp change of magnetic field orientation across the sheet (only two cells to change the polarization of magnetic field lines) and probably related to turbulent dynamics near the sheet plane. On the other side, the number of current sheet samples quickly decays with the value of δ , indicating that thick current sheets are not common in the system anymore.

Respectively, in the right plot of Figure 2 we show the evolution of distribution of the lengths of current sheet regions at the same times. As expected, initially we have one current sheet plane, extended over the whole box. This is indicated by a significant number of samples of

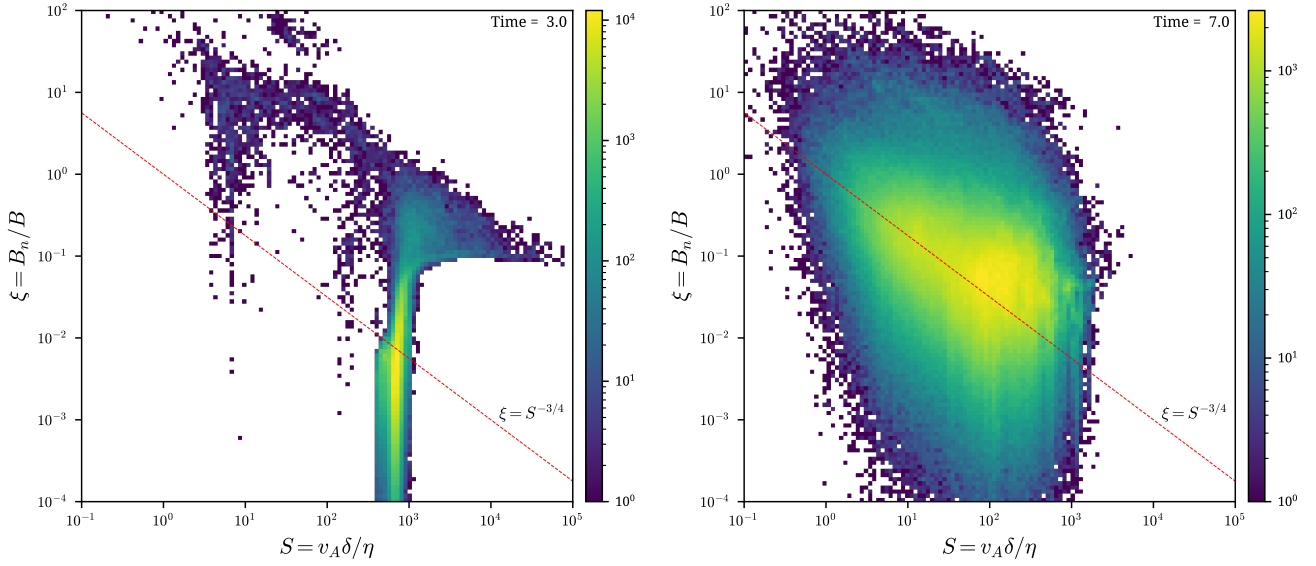


Figure 3. Correlations between the ratio of the transverse component of magnetic field to the magnetic field amplitude within the current density $\xi = B_n/B$ against the Lundquist number $S = \delta v_A/\eta$ at two evolution moments $t = 3.0$ (left) and $t = 7.0$ (right). Above the red dashed line the transverse component starts to decrease the growth rate, eventually stabilizing tearing mode.

$l \approx 1.0$ at $t = 0.1$ (blue line). However, we can also see, that at this very early time, a less significant population of samples with lengths being a fraction of L shows up. We would interpret them as the points belonging to parts of the current sheet already significantly deformed, since using our analysis, we cannot determine if these points belong to the same or separated current sheets. It is important, however, that this population increases with time, as seen at times $t = 1.0$ and 2.0 (orange and green lines, respectively). At later times, $t > 3.0$, nearly all points belong to current sheet regions with longitudinal dimension significantly shortened, comparing to the box size, with values spread between $l = 10^{-2}$ and 10^{-1} at $t = 7.0$ (purple line).

Analyzing Figure 2 we can deduce, that at initial times tearing mode should be a preferential instability for fluctuations generation, since the current sheets are characterized by relatively thin and extended current sheets with $\delta \approx 0.005 - 0.05$ and $l \lesssim 1.0$. Since $k\delta < 1.0$ for instability, it indicates that the limit for allowed wavenumbers is $k \lesssim 200$. Recalling from §3.1 the imposed perturbation wavenumber $k = 64\pi \approx 201$ at $t = 0.0$ indicates that the system should be nearly stable initially. At the final times δ decreases to values $\delta \approx 0.0002 - 0.1$, which should significantly enhance the development of tearing mode, however, the fragmentation or deformations of the current sheet decrease significantly the length l of the current sheet regions impeding the development of long wave perturbations. Still, according to the instabil-

ity condition $k\delta < 1$, perturbations with wavenumbers up to $k \approx 5000$ could be unstable.

The analysis above did not give a clear response to the question, if turbulence could be generated by tearing mode initially. At later times, the turbulence develops in regions where current sheet is thinner, potentially increasing the growth rate of the instability. At the same time, however, it is possible that the same turbulence generates component of magnetic field normal to current sheet, which, according to Eq. (3), may suppress the instability. In order to analyze the stabilizing effect of this component, we show the correlations between the normalized transverse component of magnetic field $\xi = B_n/B$ and the Lundquist number $S = v_A \delta / \eta$ in Figure 3 for two moments, $t = 3.0$ (left panel) and $t = 7.0$ (right panel). The red line, corresponding to the relation $\xi = S^{-3/4}$, divides the plot into two regions: one below the line, where ξ has negligible effect, and another above the line, where the stabilization by ξ starts to be significant and increases with the distance from the red line. In the left panel ($t = 3.0$) we see, that ξ is not important for most of the detected cells with their S values concentrated slightly below 10^3 and the parameter ξ spreading up to value 10^{-2} . A partial stabilization in the upper tail, i.e. for $\xi \approx 10^{-2} - 10^{-1}$, already takes place. We notice, that it has a characteristic increase in the direction of larger values of S at $\xi \approx 10^{-1}$. This is probably due to the broadening of the current sheet seen in the left panel of Figure 2. The points above $\xi = 1.0$,

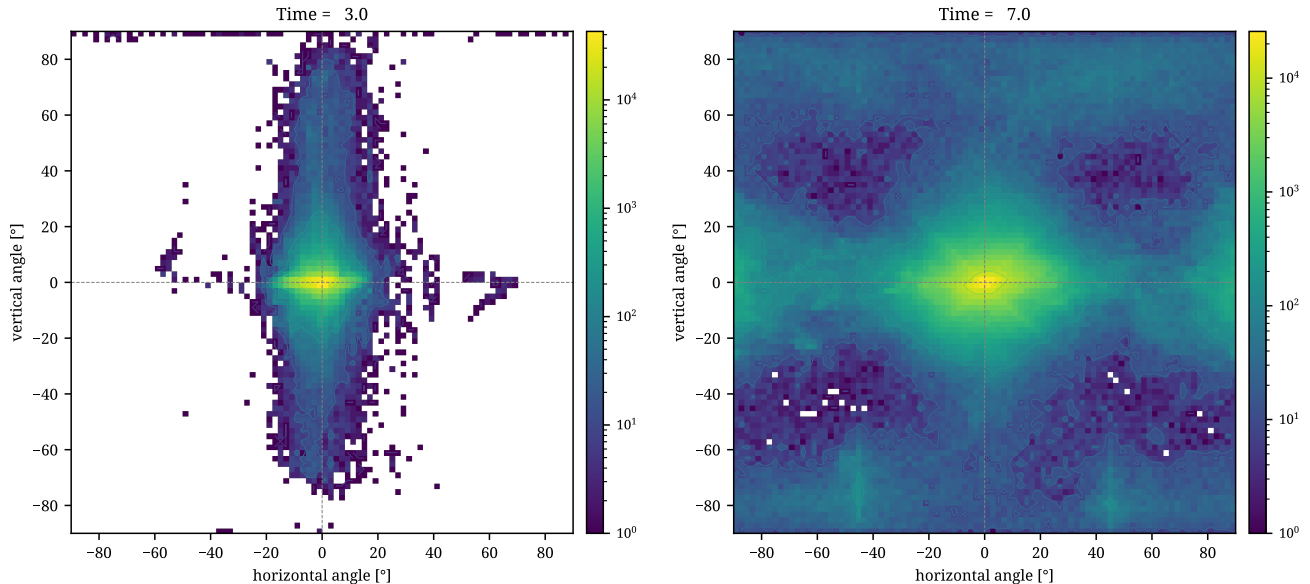


Figure 4. Distribution of the magnetic shear directions in unstable cells ($\gamma_{max} > 10^{-3}$) for the same model and moments as shown in Fig. 3. The horizontal angle corresponds to the azimuthal angle projected on the XZ plane with respect to the X axis. The vertical angle is the angle between the shear direction and the XZ plane.

although completely stabilized by ξ , are statistically insignificant.

At later time, $t = 7.0$, shown in the right panel of Figure 3, the situation is very different. The points of distribution spread toward lower values of S , roughly between 10^0 and 10^3 , and across many orders of magnitude along the stabilization parameter ξ , nearly up to 10^2 . We see a significant concentration of detected samples somewhat above the red line dividing two regions of ξ importance. Moreover, the points in the range $10^3 < S < 10^5$ disappeared nearly completely. The spread to the left along the horizontal direction should be attributed to the decrease of current sheet thicknesses due to the action of turbulence, which is also responsible for the generation of the transverse component B_n . From the distributions for two different times shown in Figure 3 we see that the generation of ξ by turbulence cannot be ignored in the estimation of the growth rate of tearing instability.

An interesting question to ask is what is the principal direction of magnetic shear in the detected current sheet cells at different moments, considering the presence of a guide field and weak initial perturbations. In Figure 4 we show the angular distribution of the shear direction only for the unstable cells (for which $\gamma_{max} > 10^{-3}$) at two moments, $t = 3.0$ (left panel) and 7.0 (right panel). We see that at $t = 3.0$ the shear direction is still strongly concentrated along the X-direction, the direction of the reconnecting component, spreading roughly from -20° to 20° in the azimuthal and from -10° to 10° in the vertical directions, with some very rare events reach-

ing even higher altitudes. At the final time, $t = 7.0$, however, the distribution of directions, although still strongly concentrated along the X axis, characterizes by a much larger spread in both directions. This indicates, that the turbulence acting on the current sheet can significantly bend it, modifying its local topology.

4.2. Kelvin–Helmholtz instability analysis

Similarly to the tearing mode analysis, we start by showing the distributions of the thickness δ and length l of the velocity shear regions in Figure 5. The first interesting observation is that there are no detected velocity shear regions for times $t = 0.1$ and 1.0 , or the shear strength is too weak, below the threshold value $U_{min} = 10^{-4}$ set in the shear detection algorithm. These distributions are of all cells at detected velocity shear maximums. At $t = 3.0$ we already see a number of cells belonging to shear regions of thicknesses δ between 2×10^{-3} and about a half of length unit, with distributions peaking at values below 10^{-2} for $t = 3.0$ and values larger than 10^{-2} at $t = 7.0$. Looking at the right panel of Figure 5 we see that the longitudinal dimensions of these shear regions spread from several cells to unity, indicating a generation of nearly global shear in the computational domain. Transforming these lengths into wavenumbers indicates, that perturbations of any k , from $k = 2\pi$ up to nearly $k \sim 5000$, may grow due to Kelvin–Helmholtz instability, if appropriate conditions are fulfilled in the local shear region. The peak value for the longitudinal dimension of shear regions is about

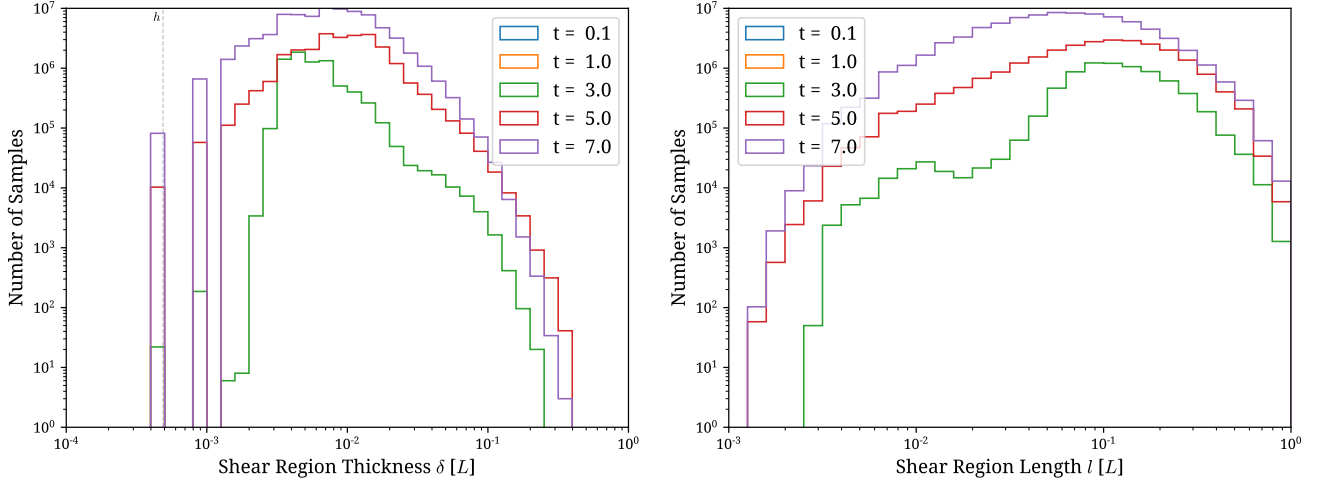


Figure 5. Statistics of the velocity shear region thickness δ (left) and length l (right) at different evolution moments, $t = 0.1, 1.0, 3.0, 5.0, 7.0$ (blue, orange, green, red, and purple, respectively). The vertical dashed line (grey) shows the effective grid size h .

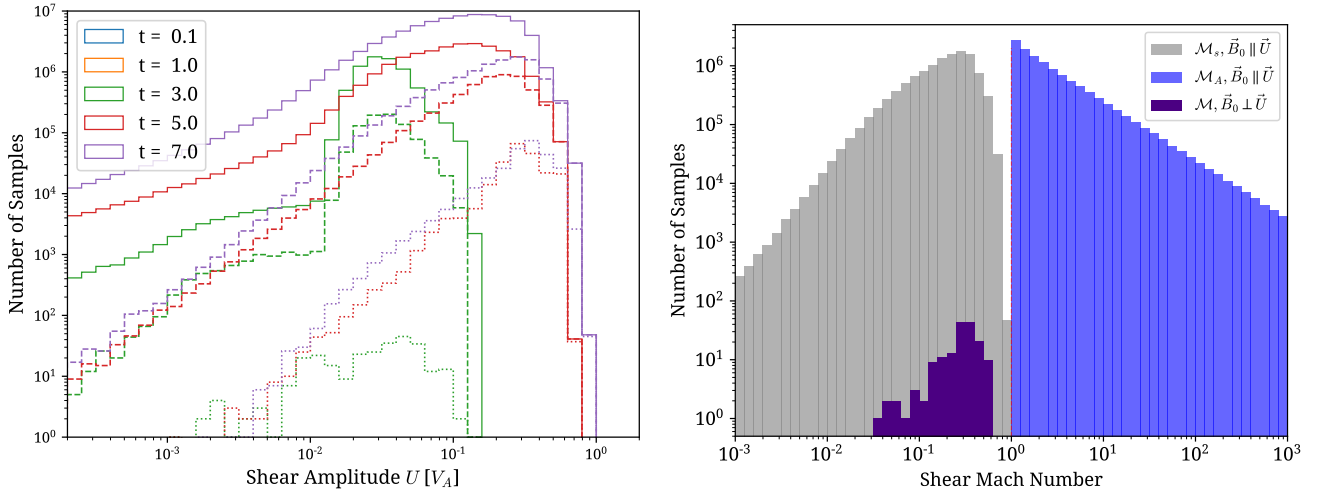


Figure 6. *Left:* Evolution of the distribution of the velocity shear strength U for different times. Solid lines correspond to all cells where shear was detected, while dashed and dotted lines correspond to the cells which are the Kelvin–Helmholtz unstable under assumption of the perturbation wavevector \vec{k} forming an angle of 0° and 75° with the shear direction, respectively. *Right:* Distribution of sonic $\mathcal{M}_s = U/a$ (grey), Alfvénic $\mathcal{M}_A = U/v_A$ (blue) and magnetosonic $\mathcal{M}_s = U/c_M$ (indigo) Mach numbers in the Kelvin–Helmholtz unstable samples at $t = 7.0$. As predicted by [Miura & Pritchett \(1982\)](#), if assuming $\vec{B}_0 \parallel \vec{U}$, $\mathcal{M}_s < 1$ and $\mathcal{M}_A > 1$ for all unstable cells, while for $\vec{B}_0 \perp \vec{U}$, $\mathcal{M} < 1$. The red dashed line corresponds to Mach number equal 1.0.

$l \sim 0.1$, decreasing slightly for later times, corresponding to the wavenumbers of $k \sim 60 - 100$.

The most important parameter in the development of the Kelvin–Helmholtz instability is the shear amplitude U . In the left panel of Figure 6 we show the evolution of distribution of U for all cells where the maximum of shear was detected (solid lines) and only for cells which are unstable with assumption that the angle between the wavevector \vec{k} and the shear direction is 0° (dashed) and 75° (dotted), according to the sufficient condition for the Kelvin–Helmholtz instability (Eq. 11). We notice, that

although the shear is relatively common after $t = 3.0$, only cells with the strongest U are in fact unstable (i.e., the corresponding growth rates determined from Eq. 10 are larger than zero). We see that for these unstable cells the shear strength spreads between 10^{-2} to nearly 1.0, measured in Alfvén speed v_A . At later times, the distribution peaks at values close to v_A . This plot clearly indicates, that strong shear can be generated in such systems in relatively short time.

In the right panel of Figure 6 we verify prediction for the compressible system by [Miura & Pritchett \(1982\)](#),

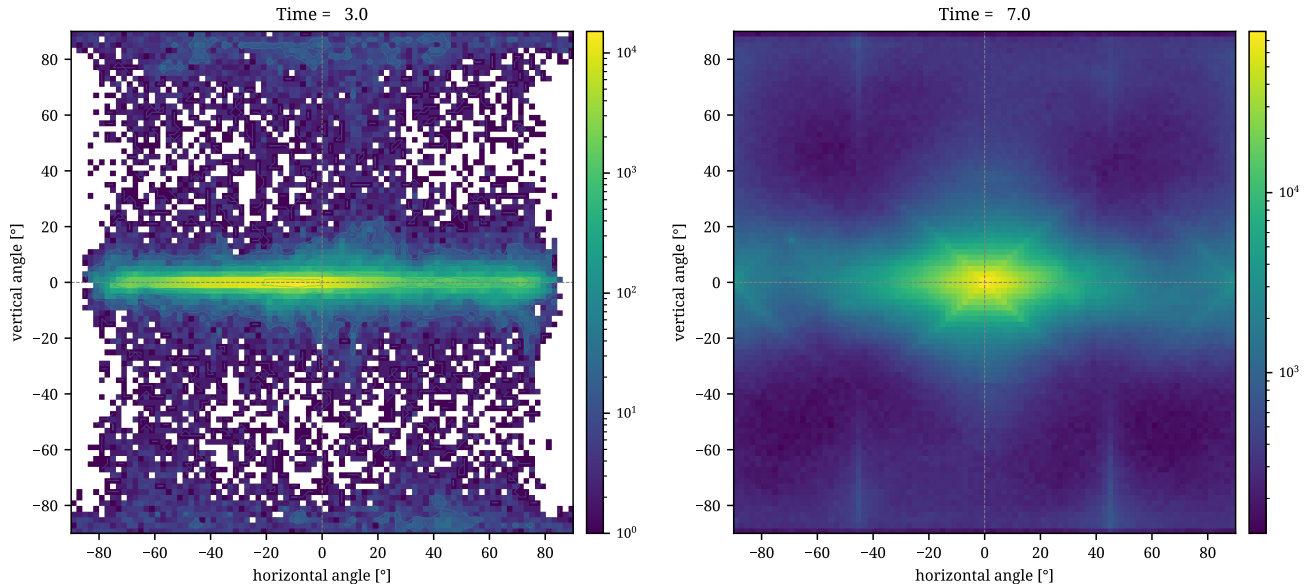


Figure 7. Distribution of the velocity shear direction in unstable cells for the same moments as shown in Fig. 3. The horizontal angle corresponds to the azimuthal angle projected on the XZ plane with respect to the X axis. The vertical angle is the angle between the shear direction and the XZ plane.

stating that if the magnetic field is parallel to the shear ($\vec{B}_0 \parallel \vec{U}$), if the sonic Mach number $\mathcal{M}_s > 1.0$ or $\mathcal{M}_A < 1.0$ the instability is stabilized. We show distributions of both Mach numbers for the last snapshot of our simulation, at $t = 7.0$. Clearly, all unstable cells have sonic Mach number $\mathcal{M}_s < 1.0$ and Alfvénic Mach number $\mathcal{M}_A > 1.0$, being in a perfect agreement with the theoretical prediction. Also, if assuming a perpendicular magnetic field ($\vec{B}_0 \perp \vec{U}$), $\mathcal{M} < 1.0$ for all unstable cells. As we can see in the right panel of Figure 6, this case agrees with the predictions too.

Similarly to tearing mode analysis, we show the distribution of velocity shear directions in Figure 7 for two moments: at $t = 3.0$ (left panel), when the Kelvin–Helmholtz unstable cells start to appear, and at the final moment $t = 7.0$ (right panel), when the instability is already developed. We see that at $t = 3.0$ the Kelvin–Helmholtz instability can operate only in the plane extended significantly in the horizontal direction from -80° to 80° and by a few degrees in the vertical one with respect to the X direction. There is also observed a small, statistically insignificant distribution of shear direction in the direction perpendicular to the shear plane. At the final time ($t = 7.0$), the velocity shear directions are scattered over all angles in both directions, azimuthal and vertical, although the most statistically significant part is within 20° from the X axis, extended somewhat more in the azimuthal direction across all angles.

4.3. Evolution of the Growth Rates: Tearing vs. Kelvin–Helmholtz

Supported by the results from previous subsections, which show the analysis of the factors important for the development of tearing and Kelvin–Helmholtz instabilities, we can now compare the estimated maximum growth rates for both instabilities. This will help us to determine which one dominates. The way we estimate γ_{max} (and corresponding k_{max}) was already described in details in §3.3 and §3.4 for tearing and Kelvin–Helmholtz instabilities, respectively. As we already have shown, the range of possible wavenumbers of perturbations, k , for both instabilities can be estimated from the longitudinal dimensions of individual shear regions, l , and the effective cell size, h . Of course, if the estimated k_{max} lays out of the allowed range, $k_l < k < k_h$, it is limited to $k_{max} = \min(\max(k_{max}, k_l), k_h)$ and a new γ_{max} is calculated accordingly. It is also important to mention, that since the dispersion relations provided in §2 were derived under certain assumptions, i.e., Eq. (6) is valid for $\xi < \alpha$ for tearing mode and Eqs. (9) and (10) (incompressible and compressible MHD, respectively) are valid for $\mathcal{M}_A^2 \gg 1$ and $\mu^2 \ll 1$, respectively, for the Kelvin–Helmholtz instability, only cells which fulfilled them were processed to obtain the results presented here.

In Figure 8 we show the distributions of estimated maximum growth rates for both instabilities. The statistics for tearing mode and Kelvin–Helmholtz instability are shown in the left and right column, respectively.

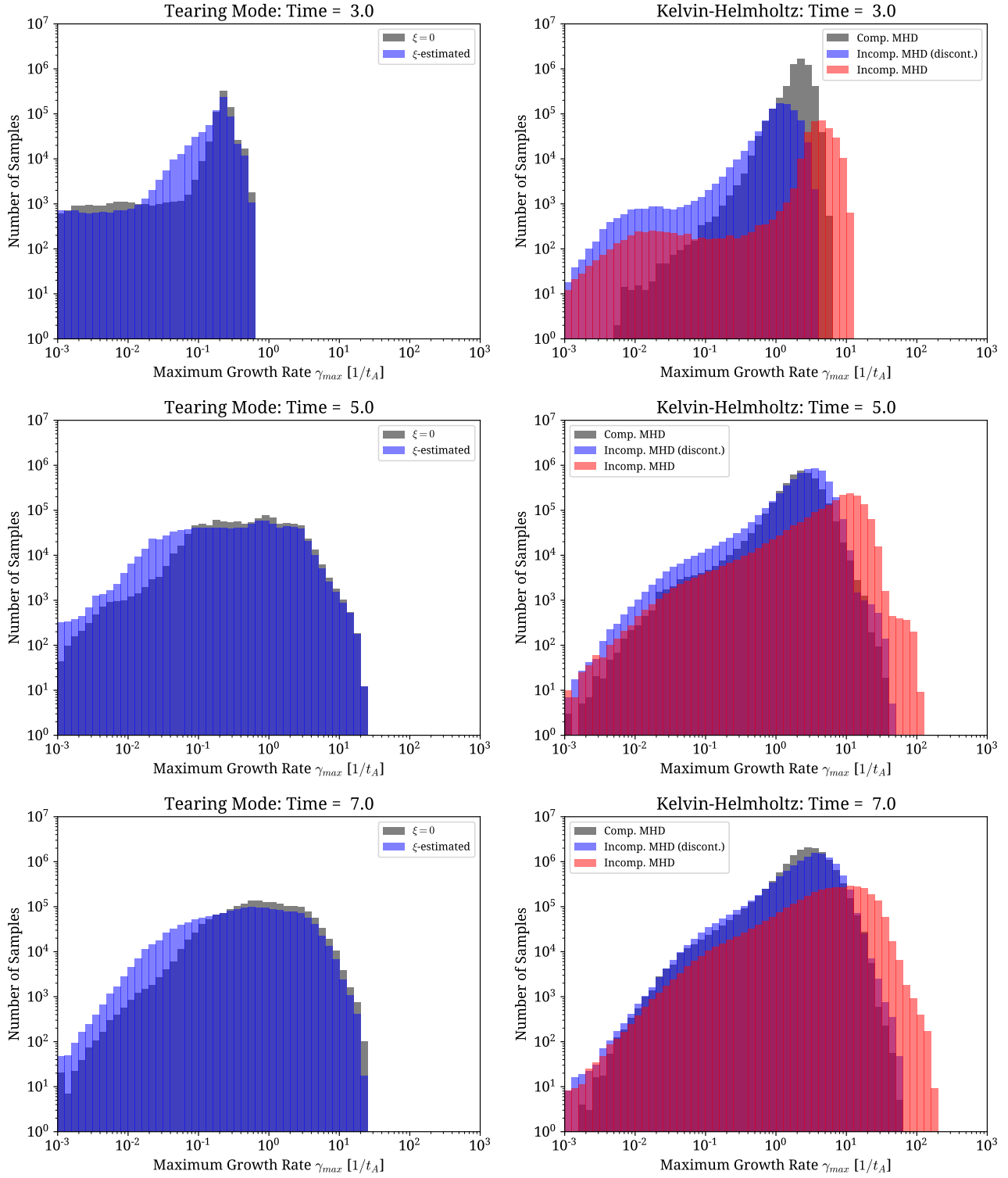


Figure 8. Evolution of the distribution of maximum growth rates for tearing mode (left) and Kelvin–Helmholtz (right) at three different times, $t = 3.0, 5.0,$ and 7.0 (upper, middle, and bottom, respectively). For tearing mode, the grey and blue distributions correspond to γ_{max} estimated from Eq. (6), with ξ set to zero and to value estimated from simulations, respectively. In the ξ -estimated distribution, only cells which fulfilled the condition $\xi < \alpha_{max}$ were taken into account. For the Kelvin–Helmholtz instability, the blue, red, and grey distributions correspond to γ_{max} estimated from Eqs. (7), (9), and (10), respectively, with the respective validity conditions taken into account.

Three different time moments were chosen, $t = 3.0, 5.0,$ and 7.0 , shown in the upper, middle, and lower rows, respectively. We see, that at earlier times (upper left panel), the tearing mode, even though expected to be a dominant one, has relatively low maximum growth rates, $\gamma_{max} < 0.7$, with the distribution peaking at $\gamma_{max} \approx 0.2 - 0.3$. We should mention that considering the initial setup, the maximum growth rate was estimated to a value ~ 0.7 at the initial current sheet. Therefore, we see a small decrease in γ_{max} at early stages. Nevertheless, the number of maximum magnetic shear cells increases at later time with the distribution of γ_{max} reaching values up to 30.0 and most of the cells characterized by $\gamma_{max} > 0.1$ (see the middle and lower left panels in Fig. 8). We should note that the distributions of the maximum growth rates for tearing instability are not too sensitive for the traverse component, represented by the parameter ξ . Even at the final time of simulation, $t = 7.0$ (the lower left panel in Fig. 8), when the turbulence is already developed in the initial current sheet region, the growth rate γ_{max} for the estimated value of ξ is reduced only in a small fraction of cells.

The Kelvin–Helmholtz instability is relatively negligible initially (see the U distribution in the left plot in Fig. 6 for $t < 30.0$). At $t = 30$ (the upper right plot in Fig. 8) the velocity shear regions have already developed and can initiate the turbulence production through the instability. As seen in the right column of Figure 8 the maximum values of γ_{max} reach $4 - 10$ depending on the used dispersion relation, with the number of cells comparable (blue and red) for incompressible MHD or even larger (grey) for compressible MHD. Taking into account the compressibility decreases γ_{max} and stabilizes the low shear regions ($U < 0.1$), as expected. However, even though the tearing mode is widespread, its maximum growth rates are smaller to those related to Kelvin–Helmholtz instability at later times. See the middle and lower panel in Figure 8 were the γ_{max} distributions for Kelvin–Helmholtz somewhat dominate those for tearing mode, both in terms of the reached growth rates and the number of detected cells.

At the final moment ($t = 7.0$), the distributions of growth rates for Kelvin–Helmholtz instability when applying the compressible MHD derivation of dispersion relation with a smooth profile and the incompressible MHD with the discontinuous profile (Eqs. 7 and 10, respectively) are very similar. Once the compressibility is ignored and a smooth shear profile considered, the instability can reach values up to nearly 200 . If we recall the distribution of Mach numbers shown in Figure 6, all unstable cells are characterized by low sonic Mach num-

bers, indicating that indeed γ_{max} could be enhanced by a factor of few.

5. DISCUSSION

5.1. Limitations of our approach

Our approach in analyzing tearing and Kelvin–Helmholtz instabilities is robust, however, it has its drawbacks, which should be pointed out. First of all, in the presence of growing turbulent fluctuations, it is nearly impossible to determine the characteristics of the perturbations present in the analyzed local shear region. In order to determine the growth rate precisely, we would have to possess information about the wavenumber and direction of each local perturbation. In order to compensate the lack of these data, we determine the plausible range of wavenumbers for which the instabilities would have been unstable. Therefore, they are limited to the range $k \in (k_l, k_h)$ as described in §3.3 for tearing and §3.4 for Kelvin–Helmholtz instabilities. In the derivation of the maximum growth rates γ_{max} we determine the corresponding perturbation wavenumber k_{max} . If this wavenumber lays out of the range (k_l, k_h) , it is limited and the growth rate is calculated directly from the dispersion relations. Moreover, we apply all the conditions related to stability and the validity of dispersion relations. However, the condition for the stability of the Kelvin–Helmholtz depends on the direction of perturbation and upstream magnetic field. In the derivation of γ_{max} we assume $\vec{k} \parallel \vec{U}$, using the fact that the initial perturbation was isotropic, and once the turbulence is developed it is possible to find modes parallel to the shear.

As we described in the beginning of §4 our results are based on the statistics extracted from the cell by cell analysis and the data were collected only for cells belonging to shear maximums. It means that the measurement do not represent the individual shear regions and for which the analysis is done separately. For example, in the case of tearing instability analysis, we have one current sheet initially crossing the whole computational box, therefore the points represent the cells along the plane of the maximum of current density. Due to the developing turbulence, this current sheet is being deformed and eventually broken into a number of current sheet regions, not necessarily separated, but interlinked in a complex manner. Therefore, our analysis should be understood as a comparative one between two instabilities. This should be kept in mind especially when interpreting the statistics of longitudinal dimensions of shear regions.

The derivation of analytical dispersion relations for tearing and Kelvin–Helmholtz instabilities requires sig-

nificant simplifications. Usually a two uniform regions of density, pressure, magnetic field and velocity are considered connected by transition layer. This layer can be discontinuous or smooth. The smooth case is usually approximated by a piecewise linear or hyperbolic tangent profile. The dispersion relations are different for these three different profiles, giving different dependence of the growth rate γ on the perturbation wavenumber k (see, e.g., Furth et al. 1963; Somov & Verneva 1989; Chandrasekhar 1961; Ong & Roderick 1972; Walker 1981; Miura & Pritchett 1982; Chen et al. 1997; Berlok & Pfrommer 2019). For a discontinuous profile ($\delta \approx 0$) there is no limit on the wavenumber. The condition $k\delta < 1$ is always fulfilled in the case of tearing mode, and the growth rate of Kelvin–Helmholtz instability depends linearly on k , resulting in arbitrary large values of γ . Taking into account a smooth transition within the shear region results in the existence of the wavenumber k_{max} for which the growth rate has its maximum γ_{max} , and which typically is related to the thickness of the region $k\delta \approx 1$. This maximum growth rate is usually a fraction of the growth rate corresponding to the discontinuous shear. It is relatively difficult to determine the exact profile in the shear regions detected in our simulation. Specially in the case of broad shear and in the presence of turbulence the profile can be very different from piecewise linear or hyperbolic tangent ones. Nevertheless, after determining the thickness δ and upstream fields, \vec{B}_0 and \vec{U} , we assumed they represent the finite width profiles used in derivation of the corresponding to each instability dispersion relation. Moreover, in the calculation of tearing growth rates we did not take into account the compressibility, although its effect should be relatively negligible, since the velocity fluctuations do not reach velocities larger than the sound speed a .

5.2. Turbulent reconnection as a dominant process

Suggested 20 years ago, the turbulent reconnection model has gotten significant support both from subsequent numerical (see Kowal et al. 2009, 2012, 2017; Eyink et al. 2013; Oishi et al. 2015; Takamoto et al. 2015; Beresnyak 2017; Takamoto 2018), theoretical (Eyink et al. 2011; Eyink 2011, 2015; Lazarian et al. 2015, 2019), as well as observational (see Ciaravella & Raymond 2008; Sych et al. 2009, 2015; Khabarova & Obridko 2012; Lazarian et al. 2012; Santos-Lima et al. 2013; Leão et al. 2013; González-Casanova et al. 2018) studies. At the moment of its introduction the model was an alternative to the Hall-MHD models predicting Petschek X-point geometry of reconnection point, i.e., very regular type of reconnection. The later model required plasma to be collisionless, which is in contrast to the turbu-

lent one, which did not depend on any plasma microphysics and was applicable to both collisional and collisionless media. It was later understood that the X-point geometry is not tenable in realistic settings. Instead, the tearing reconnection (see Syrovatskii 1981; Loureiro et al. 2007; Bhattacharjee et al. 2009) became the main alternative scenario for the turbulent model. So far 2-dimensional simulations demonstrated fast reconnection for both MHD and kinetic regimes. Compared to earlier Hall-MHD reconnection that necessarily required collisionless plasma condition this was definitely an important improvement. The tearing reconnection shares many features with the turbulent one. For instance, Hall-MHD Petschek-type reconnection, due to the presence of slow shock crossing the boundary, required a particular set of boundary conditions that was difficult to preserve in the realistic setting with the random external perturbations (see, e.g. Forbes 2001). In the presence of random/turbulent motions, inevitable in astrophysical settings, the Petschek solution would not be satisfied. The tearing plasmoid reconnection is a more robust scheme therefore.

With two reconnection processes providing fast reconnection, it is important to understand the applicability of each. It has been numerically demonstrated in Kowal et al. (2009) that including additional microscopic effects simulating enhanced plasma resistivity does not change the turbulent reconnection rate. This agrees well with the theoretical expectations in turbulent reconnection (see LV99 and Eyink 2011), in particular with the generalized Ohm’s law derived in Eyink (2015). As a result, if media is already turbulent, one does not expect to see effects of tearing reconnection. With the existing observational evidence about the turbulence of astrophysical fluids this means that the turbulent reconnection is dominant for most of the cases. For instance, we expect the turbulent reconnection to govern violation of the flux freezing in turbulent fluids. This results in reconnection diffusion that governs star formation (Lazarian et al. 2012), induces the violations of the structure of the heliospheric current sheet and the Parker spiral (Eyink 2015).

The numerical results on flux freezing violation that follows from the LV99 theory cannot be possibly explained with the tearing reconnection. This clearly demonstrates that there are situations when the turbulent reconnection is at work, while tearing reconnection is not expected.

The “pure” problem of self-driven turbulent reconnection was the focus of our study in Kowal et al. (2017). There we showed that in the absence of the external turbulence driving the turbulence develops in the reconnect-

tion region and this turbulence has the properties corresponding to the expectations of the MHD turbulence. This was in contrast to [Huang & Bhattacharjee \(2016\)](#) who claimed that turbulence produced in reconnection regions is radically different from the [Goldreich & Sridhar \(1995\)](#) one. The properties of turbulence are important, as the LV99 magnetic reconnection and closely connected to it Richardson dispersion ([Eyink et al. 2011](#)) are proven to work in conditions where no tearing instability is expected. Therefore, if such type of turbulence is present in the reconnection regions it is expected to induce fast reconnection. The correspondence of the reconnection rates in self-driven reconnection with the expectations of the LV99 theory was demonstrated in [Lazarian et al. \(2015\)](#), where the results of earlier simulations, e.g. [Beresnyak \(2013\)](#), were analyzed.

The present paper is a step forward in understanding the process of self-induced fast reconnection. Here we explore the nature of turbulence driving in the reconnection region. If tearing mode is absolutely essential for driving turbulence, one may still argue that the actual reconnection is happening via tearing, while the turbulence is playing only an auxiliary role for the process. Our results, in fact, testify that the actual picture is very different. The process of tearing mode plays in 3D a role at the earliest stage of reconnection. As the system evolves in time the outflows induced by the reconnection region become turbulent, with Kelvin-Helmholtz instability playing the dominant role. As the reconnection grows, the region becomes more and more turbulent with the tearing instability being overtaken or even suppressed, not playing a role on the reconnection process overall.

Our simulations are performed in the high beta plasma regime and in such conditions the reconnection outflow does not induce sufficient turbulence to trigger the self-accelerating process of "reconnection instability" (see [Lazarian & Vishniac 2009](#)) though.

While the MHD simulations show a very different picture for 2D and 3D self-driven reconnection, the particles-in-cell (PIC) simulations tend to show similar tearing patterns both in 3D and 2D. One possible explanation is related to limitations of present-day PIC simulation, given that these do not present enough particles in the reconnection regions to result in developed turbulence. Therefore, in such "viscous" regime the Kelvin-Helmholtz instability is suppressed and cannot operate and the only signatures that can be seen arise from the tearing instability. In other words, the "viscous" outflow does not feel the additional degrees of freedom that would allow high Reynolds turbulent behavior to take place. Nevertheless, the high resolution PIC simula-

tions presented by Hui Li in a reconnection review by [Lazarian et al. \(2019\)](#) show the signatures of developing turbulence, e.g., the Richardson dispersion of magnetic field lines was reported. Therefore, we expect that the results we now obtained with MHD modelling can be also obtained/confirmed with very high particle number PIC simulations.

There is, however, another puzzle that is presented by the comparison of the 3D kinetic and MHD simulations. The kinetic simulations show higher reconnection rates and it is important to understand whether these differences persist for reconnection at all scales or they are just a transient feature of reconnection processes taking place for small-scale reconnection. This issue was recently addressed in [Beresnyak \(2018\)](#) using Hall-MHD code. The results there testify that the reconnection rates for self-driven 3D turbulent reconnection obtained with Hall-MHD gradually converge to the results obtained for the 3D MHD self-driven reconnection. This is what one expects from the theory (see LV99; [Eyink et al. 2011](#); [Eyink 2015](#)). Nevertheless, in terms of our present study the convergence of the results obtained with MHD and Hall-MHD code testify that the results in the present paper will not change in the presence of additional plasma effects.

Our confirmation of the predictions of turbulent reconnection theory formulated in the LV99, and subsequent theoretical studies, also has bearing on the ongoing discussion of the so called "reconnection-mediated turbulence" idea presented in a number of theoretical papers (see [Loureiro & Boldyrev 2017a,b](#); [Boldyrev & Loureiro 2017, 2018](#); [Walker et al. 2018](#); [Mallet et al. 2017b,a](#); [Comisso et al. 2018](#); [Vech et al. 2018](#)). For sufficiently large Reynolds numbers, due to both the process of "dynamical alignment" and the effect of magnetic fluctuations getting more anisotropic with the decrease of the scale, the current sheets prone to tearing instability can develop. Such changes of the turbulence at the scale λ_c in the vicinity of the dissipation scale do not change the nature of turbulent cascade, which lies on scales of the inertial range $\gg \lambda_c$. Our study is therefore suggestive that if reconnection takes place at small scales, comparable to λ_c , it will also be turbulent as demonstrated by our simulations. However, since reconnection does not happen at the larger eddies scales it is preferred to refer this hypothetical regime as "tearing-mediated turbulence" instead. The objective reality is, however, that in the reconnection community historically only bursts of reconnection was considered.

6. CONCLUSIONS

In this work we analyzed two MHD instabilities: tearing mode and Kelvin–Helmholtz, which are candidates for processes responsible for turbulence generation in spontaneous reconnection, e.g. the reconnection without externally imposed turbulent driving. The generated turbulence is due to the initially imposed weak noise present in the vicinity of the Harris current sheet. We analyzed factors important for growth of both instabilities, but also those which suppress them. The analysis presented in this work has shown important results which can be synthesized in the following:

- The region of current sheet with the presence of initial noise develops into a region with conditions favorable for development of MHD instabilities, such as tearing mode or Kelvin–Helmholtz instability. Although the tearing instability is natural for thin elongated current sheets, the conditions for Kelvin–Helmholtz instability have never been verified before in systems with stochastic reconnection.
- Evolution of stochastic reconnection leads to formation of shear regions, both magnetic and velocity, with broad range of thicknesses and longitudinal dimensions. Our studies indicate that the regions of magnetic shear for later times are somewhat thinner comparing to those of velocity shear, while the longitudinal scales of these regions are shorter for velocity shear comparing to the magnetic one.
- Tearing instability is expected to develop at earlier stages, while, once a sufficient amplitude of turbulence is generated near the current sheet, it can be suppressed due to the presence of the transverse component of magnetic field B_n . As shown in [Somov & Vernet \(1993\)](#), for $\xi = B_n/B > S^{-3/4}$ this

instability is suppressed. We demonstrate that in our models ξ can be sufficiently large but does not completely suppress the instability. Taking into account the contribution of transverse component B_n , the instability can develop with dynamical time shorter than the Alfvénic time t_A under favorable circumstances. The estimated maximum growth rate γ_{max} , initially below unity, reaches values of a few tens at later times with the most of detected points laying in the range 0.1 – 10.

- Due to misalignment of the outflows from neighboring reconnection events, they can generate enough sheared flows to induce Kelvin–Helmholtz instability. The Mach numbers calculated with respect to the shear velocity U satisfy necessary conditions for the instability to develop. Our analysis indicates the presence of sheared regions with broad range of amplitudes, $10^{-2} \leq U \leq 1$, and thicknesses, $10^{-3} \leq \delta \leq 0.5$. The distributions of the estimated maximum growth rates γ_{max} peak at values between 1 – 10 and reaching maximum values close to 100, suggest the growth of Kelvin–Helmholtz instability (within the dynamical time) much shorter than the time t_A .

G.K. acknowledges support from CNPq (no. 304891/2016-9). D.F.G. thanks the Brazilian agencies CNPq (no. 311128/2017-3) and FAPESP (no. 2013/10559-5) for financial support. A.L. acknowledges the NSF grant 1816234 and NASA TCAN 144AAG1967. E.T.V. acknowledges the support of the AAS. This work has made use of the computing facilities the Academic Supercomputing Center in Kraków, Poland (Supercomputer Prometheus at ACK CYFRONET AGH) and of the Laboratory of Astrophysics (EACH/USP, Brazil).

REFERENCES

- Alfvén, H. 1942, *Nature*, 150, 405, doi: [10.1038/150405d0](https://doi.org/10.1038/150405d0)
- Ara, G., Basu, B., Coppi, B., et al. 1978, *Annals of Physics*, 112, 443, doi: [10.1016/S0003-4916\(78\)80007-4](https://doi.org/10.1016/S0003-4916(78)80007-4)
- Armstrong, J. W., Rickett, B. J., & Spangler, S. R. 1995, *ApJ*, 443, 209, doi: [10.1086/175515](https://doi.org/10.1086/175515)
- Beresnyak, A. 2013, ArXiv e-prints. <https://arxiv.org/abs/1301.7424>
- . 2017, *ApJ*, 834, 47, doi: [10.3847/1538-4357/834/1/47](https://doi.org/10.3847/1538-4357/834/1/47)
- Beresnyak, A. 2018, in *Journal of Physics Conference Series*, Vol. 1031, *Journal of Physics Conference Series*, 012001
- Berlok, T., & Pfrommer, C. 2019, *MNRAS*, 485, 908, doi: [10.1093/mnras/stz379](https://doi.org/10.1093/mnras/stz379)
- Bhattacharjee, A., Huang, Y.-M., Yang, H., & Rogers, B. 2009, *Physics of Plasmas*, 16, 112102, doi: [10.1063/1.3264103](https://doi.org/10.1063/1.3264103)
- Boldyrev, S., & Loureiro, N. F. 2017, *ApJ*, 844, 125, doi: [10.3847/1538-4357/aa7d02](https://doi.org/10.3847/1538-4357/aa7d02)
- Boldyrev, S., & Loureiro, N. F. 2018, in *Journal of Physics Conference Series*, Vol. 1100, *Journal of Physics Conference Series*, 012003
- Chandrasekhar, S. 1961, *Hydrodynamic and hydromagnetic stability* (Oxford)
- Chen, Q., Otto, A., & Lee, L. C. 1997, *J. Geophys. Res.*, 102, 151, doi: [10.1029/96JA03144](https://doi.org/10.1029/96JA03144)

- Chepurnov, A., Burkhart, B., Lazarian, A., & Stanimirovic, S. 2015, *ApJ*, 810, 33, doi: [10.1088/0004-637X/810/1/33](https://doi.org/10.1088/0004-637X/810/1/33)
- Chepurnov, A., & Lazarian, A. 2010, *ApJ*, 710, 853, doi: [10.1088/0004-637X/710/1/853](https://doi.org/10.1088/0004-637X/710/1/853)
- Ciaravella, A., & Raymond, J. C. 2008, *ApJ*, 686, 1372, doi: [10.1086/590655](https://doi.org/10.1086/590655)
- Comisso, L., Huang, Y. M., Lingam, M., Hirvijoki, E., & Bhattacharjee, A. 2018, *ApJ*, 854, 103, doi: [10.3847/1538-4357/aaac83](https://doi.org/10.3847/1538-4357/aaac83)
- Coppi, B., Galvao, R., Pellat, R., Rosenbluth, M., & Rutherford, P. 1976, *Soviet Journal of Plasma Physics*, 2, 533
- Dougherty, R. L., Edelman, A. S., & Hyman, J. M. 1989, *Mathematics of Computation*, 52, 471–494, doi: [10.1090/S0025-5718-1989-0962209-1](https://doi.org/10.1090/S0025-5718-1989-0962209-1)
- Drazin, P. G., & Reid, W. H. 1981, *NASA STI/Recon Technical Report A*, 82, 17950
- Eyink, G., Vishniac, E., Lalescu, C., et al. 2013, *Nature*, 497, 466, doi: [10.1038/nature12128](https://doi.org/10.1038/nature12128)
- Eyink, G. L. 2011, *PhRvE*, 83, 056405, doi: [10.1103/PhysRevE.83.056405](https://doi.org/10.1103/PhysRevE.83.056405)
- . 2015, *ApJ*, 807, 137, doi: [10.1088/0004-637X/807/2/137](https://doi.org/10.1088/0004-637X/807/2/137)
- Eyink, G. L., Lazarian, A., & Vishniac, E. T. 2011, *ApJ*, 743, 51, doi: [10.1088/0004-637X/743/1/51](https://doi.org/10.1088/0004-637X/743/1/51)
- Faganello, M., & Califano, F. 2017, *Journal of Plasma Physics*, 83, 535830601, doi: [10.1017/S0022377817000770](https://doi.org/10.1017/S0022377817000770)
- Fejer, J. A. 1964, *Physics of Fluids*, 7, 499, doi: [10.1063/1.1711229](https://doi.org/10.1063/1.1711229)
- Forbes, T. G. 2001, *Earth, Planets, and Space*, 53, 423, doi: [10.1186/BF03353252](https://doi.org/10.1186/BF03353252)
- Frank, A., Jones, T. W., Ryu, D., & Gaalaas, J. B. 1996, *ApJ*, 460, 777, doi: [10.1086/177009](https://doi.org/10.1086/177009)
- Furth, H. P., Killeen, J., & Rosenbluth, M. N. 1963, *Physics of Fluids*, 6, 459, doi: [10.1063/1.1706761](https://doi.org/10.1063/1.1706761)
- Galeev, A. A., & Zelenyi, L. M. 1975, *Soviet Journal of Experimental and Theoretical Physics Letters*, 22, 170
- . 1976, *Soviet Journal of Experimental and Theoretical Physics*, 43, 1113
- Gerwin, R. A. 1968, *Reviews of Modern Physics*, 40, 652, doi: [10.1103/RevModPhys.40.652](https://doi.org/10.1103/RevModPhys.40.652)
- Goldreich, P., & Sridhar, S. 1995, *ApJ*, 438, 763, doi: [10.1086/175121](https://doi.org/10.1086/175121)
- González-Casanova, D. F., Lazarian, A., & Cho, J. 2018, *MNRAS*, 475, 3324, doi: [10.1093/mnras/sty006](https://doi.org/10.1093/mnras/sty006)
- Greco, A., Chuychai, P., Matthaeus, W. H., Servidio, S., & Dmitruk, P. 2008, *Geophys. Res. Lett.*, 35, L19111, doi: [10.1029/2008GL035454](https://doi.org/10.1029/2008GL035454)
- Gudkov, M. G., & Troshichev, O. A. 1996, *Journal of Atmospheric and Terrestrial Physics*, 58, 613, doi: [10.1016/0021-9169\(95\)00082-8](https://doi.org/10.1016/0021-9169(95)00082-8)
- Huang, Y.-M., & Bhattacharjee, A. 2016, *ApJ*, 818, 20, doi: [10.3847/0004-637X/818/1/20](https://doi.org/10.3847/0004-637X/818/1/20)
- Jacobson, A. R., & Moses, R. W. 1984, *PhRvA*, 29, 3335, doi: [10.1103/PhysRevA.29.3335](https://doi.org/10.1103/PhysRevA.29.3335)
- Khabarova, O., & Obridko, V. 2012, *ApJ*, 761, 82, doi: [10.1088/0004-637X/761/2/82](https://doi.org/10.1088/0004-637X/761/2/82)
- Kiefer, J. 1953, *Proceedings of the American Mathematical Society*, 4, 502, doi: [10.1090/S0002-9939-1953-0055639-3](https://doi.org/10.1090/S0002-9939-1953-0055639-3)
- Kowal, G., Falceta-Gonçalves, D. A., Lazarian, A., & Vishniac, E. T. 2017, *ApJ*, 838, 91, doi: [10.3847/1538-4357/aa6001](https://doi.org/10.3847/1538-4357/aa6001)
- Kowal, G., Lazarian, A., Vishniac, E. T., & Otmianowska-Mazur, K. 2009, *ApJ*, 700, 63, doi: [10.1088/0004-637X/700/1/63](https://doi.org/10.1088/0004-637X/700/1/63)
- . 2012, *Nonlinear Processes in Geophysics*, 19, 297, doi: [10.5194/npg-19-297-2012](https://doi.org/10.5194/npg-19-297-2012)
- Lazarian, A. 2005, in *American Institute of Physics Conference Series*, Vol. 784, *Magnetic Fields in the Universe: From Laboratory and Stars to Primordial Structures.*, ed. E. M. de Gouveia dal Pino, G. Lugones, & A. Lazarian, 42–53
- Lazarian, A., Esquivel, A., & Crutcher, R. 2012, *ApJ*, 757, 154, doi: [10.1088/0004-637X/757/2/154](https://doi.org/10.1088/0004-637X/757/2/154)
- Lazarian, A., Eyink, G., Jafari, A., et al. 2019, *Physics of Plasmas*
- Lazarian, A., Eyink, G., Vishniac, E., & Kowal, G. 2015, *Philosophical Transactions of the Royal Society of London Series A*, 373, 20140144, doi: [10.1098/rsta.2014.0144](https://doi.org/10.1098/rsta.2014.0144)
- Lazarian, A., & Vishniac, E. T. 1999, *ApJ*, 517, 700, doi: [10.1086/307233](https://doi.org/10.1086/307233)
- Lazarian, A., & Vishniac, E. T. 2009, in *Revista Mexicana de Astronomía y Astrofísica Conference Series*, Vol. 36, *Magnetic Fields in the Universe II: From Laboratory and Stars to the Primordial Universe*, ed. A. Esquivel, J. Franco, G. García-Segura, E. M. de Gouveia Dal Pino, A. Lazarian, S. Lizano, & A. Raga, 81–88
- Leão, M. R. M., de Gouveia Dal Pino, E. M., Santos-Lima, R., & Lazarian, A. 2013, *ApJ*, 777, 46, doi: [10.1088/0004-637X/777/1/46](https://doi.org/10.1088/0004-637X/777/1/46)
- Loureiro, N. F., & Boldyrev, S. 2017a, *PhRvL*, 118, 245101, doi: [10.1103/PhysRevLett.118.245101](https://doi.org/10.1103/PhysRevLett.118.245101)
- . 2017b, *ApJ*, 850, 182, doi: [10.3847/1538-4357/aa9754](https://doi.org/10.3847/1538-4357/aa9754)
- Loureiro, N. F., Schekochihin, A. A., & Cowley, S. C. 2007, *Physics of Plasmas*, 14, 100703, doi: [10.1063/1.2783986](https://doi.org/10.1063/1.2783986)
- Loureiro, N. F., Schekochihin, A. A., & Uzdensky, D. A. 2013, *PhRvE*, 87, 013102, doi: [10.1103/PhysRevE.87.013102](https://doi.org/10.1103/PhysRevE.87.013102)

- Mallet, A., Schekochihin, A. A., & Chandran, B. D. G. 2017a, *Journal of Plasma Physics*, 83, 905830609, doi: [10.1017/S0022377817000812](https://doi.org/10.1017/S0022377817000812)
- Mallet, A., Schekochihin, A. A., & Chandran, B. D. G. 2017b, *MNRAS*, 468, 4862, doi: [10.1093/mnras/stx670](https://doi.org/10.1093/mnras/stx670)
- Matthaeus, W. H., & Lamkin, S. L. 1985, *Physics of Fluids*, 28, 303, doi: [10.1063/1.865147](https://doi.org/10.1063/1.865147)
- . 1986, *Physics of Fluids*, 29, 2513, doi: [10.1063/1.866004](https://doi.org/10.1063/1.866004)
- Michalke, A. 1964, *Journal of Fluid Mechanics*, 19, 543, doi: [10.1017/S0022112064000908](https://doi.org/10.1017/S0022112064000908)
- Miura, A., & Pritchett, P. L. 1982, *J. Geophys. Res.*, 87, 7431, doi: [10.1029/JA087iA09p07431](https://doi.org/10.1029/JA087iA09p07431)
- Oishi, J. S., Mac Low, M.-M., Collins, D. C., & Tamura, M. 2015, *ApJL*, 806, L12, doi: [10.1088/2041-8205/806/1/L12](https://doi.org/10.1088/2041-8205/806/1/L12)
- Ong, R. S. B., & Roderick, N. 1972, *Planet. Space Sci.*, 20, 1, doi: [10.1016/0032-0633\(72\)90135-3](https://doi.org/10.1016/0032-0633(72)90135-3)
- Padoan, P., Juvela, M., Kritsuk, A., & Norman, M. L. 2009, *ApJL*, 707, L153, doi: [10.1088/0004-637X/707/2/L153](https://doi.org/10.1088/0004-637X/707/2/L153)
- Parker, E. N. 1957, *J. Geophys. Res.*, 62, 509, doi: [10.1029/JZ062i004p00509](https://doi.org/10.1029/JZ062i004p00509)
- Petschek, H. E. 1964, *NASA Special Publication*, 50, 425
- Rayleigh, L. 1879, *Proceedings of the London Mathematical Society*, s1-11, 57, doi: [10.1112/plms/s1-11.1.57](https://doi.org/10.1112/plms/s1-11.1.57)
- Santos-Lima, R., de Gouveia Dal Pino, E. M., & Lazarian, A. 2013, *MNRAS*, 429, 3371, doi: [10.1093/mnras/sts597](https://doi.org/10.1093/mnras/sts597)
- Santos-Lima, R., Lazarian, A., de Gouveia Dal Pino, E. M., & Cho, J. 2010, *ApJ*, 714, 442, doi: [10.1088/0004-637X/714/1/442](https://doi.org/10.1088/0004-637X/714/1/442)
- Schindler, K. 1974, *J. Geophys. Res.*, 79, 2803, doi: [10.1029/JA079i019p02803](https://doi.org/10.1029/JA079i019p02803)
- Sen, A. K. 1964, *Physics of Fluids*, 7, 1293, doi: [10.1063/1.1711374](https://doi.org/10.1063/1.1711374)
- Servidio, S., Dmitruk, P., Greco, A., et al. 2011, *Nonlinear Processes in Geophysics*, 18, 675, doi: [10.5194/npg-18-675-2011](https://doi.org/10.5194/npg-18-675-2011)
- Somov, B. V., & Verneta, A. I. 1989, *SoPh*, 120, 93, doi: [10.1007/BF00148536](https://doi.org/10.1007/BF00148536)
- . 1993, *SSRv*, 65, 253, doi: [10.1007/BF00754510](https://doi.org/10.1007/BF00754510)
- Sweet, P. A. 1958, *The Observatory*, 78, 30
- Sych, R., Karlický, M., Altyntsev, A., Dudík, J., & Kashapova, L. 2015, *A&A*, 577, A43, doi: [10.1051/0004-6361/201424834](https://doi.org/10.1051/0004-6361/201424834)
- Sych, R., Nakariakov, V. M., Karlicky, M., & Anfinogentov, S. 2009, *A&A*, 505, 791, doi: [10.1051/0004-6361/200912132](https://doi.org/10.1051/0004-6361/200912132)
- Syrovatskii, S. I. 1981, *ARA&A*, 19, 163, doi: [10.1146/annurev.aa.19.090181.001115](https://doi.org/10.1146/annurev.aa.19.090181.001115)
- Takamoto, M. 2018, *MNRAS*, 476, 4263, doi: [10.1093/mnras/sty493](https://doi.org/10.1093/mnras/sty493)
- Takamoto, M., Inoue, T., & Lazarian, A. 2015, *ApJ*, 815, 16, doi: [10.1088/0004-637X/815/1/16](https://doi.org/10.1088/0004-637X/815/1/16)
- Vech, D., Mallet, A., Klein, K. G., & Kasper, J. C. 2018, *ApJL*, 855, L27, doi: [10.3847/2041-8213/aab351](https://doi.org/10.3847/2041-8213/aab351)
- Walker, A. D. M. 1981, *Planet. Space Sci.*, 29, 1119, doi: [10.1016/0032-0633\(81\)90011-8](https://doi.org/10.1016/0032-0633(81)90011-8)
- Walker, J., Boldyrev, S., & Loureiro, N. F. 2018, *PhRvE*, 98, 033209, doi: [10.1103/PhysRevE.98.033209](https://doi.org/10.1103/PhysRevE.98.033209)